5-14-2024

Application of Finite-State Wake Models to Rotors Re-entering Their Own Wake

Michael Seay Morrow
Washington University – McKelvey School of Engineering

WASHINGTON UNIVERSITY IN ST. LOUIS

McKelvey School of Engineering

Department of Mechanical Engineering & Materials Science

Dissertation Examination Committee:

David A. Peters, Chair

Richard Axelbaum

Philip Bayly

Mark Jakiela

Swami Karunamoorthy

Application of Finite-State Wake Models to Rotors Re-entering Their Own Wake

by

Michael Seay Morrow

A dissertation presented to

the McKelvey School of Engineering

of Washington University in

partial fulfillment of the

requirements for the degree

of Doctor of Philosophy

May 2024

St. Louis, Missouri

Table of Contents

List of Figures

List of Tables

List of Symbols

$\hat{a}_n^m$	=	Cosine Induced Inflow Expansion Coefficients
$\hat{b}_n^m$	=	Sine Induced Inflow Expansion Coefficients
$[D]$	=	Damping Matrix
e	=	Internal Energy per Unit Mass
$\vec{f}$	=	External Forces
k	=	Thermal Conductivity of the Fluid
$[L]$	=	Influence Coefficient Matrix
$[M]$	=	Apparent Mass Matrix
P	=	Nondimensional Pressure
p	=	Pressure of Fluid
$\bar{P}_n^m$	=	Normalized Legendre Function of the First Kind
$\bar{Q}_n^m$	=	Normalized Legendre Function of the Second Kind
T	=	Fluid Temperature
t	=	Time
$\bar{t}$	=	Nondimensional Time
$\vec{v}$	=	Nondimensional Perturbation Velocity
V	=	Nondimensional Freestream Velocity
V_∞	=	Steady Freestream Velocity
$\vec{v}_t$	=	Total Velocity Vector of Fluid
$\delta\vec{v}$	=	Perturbation Velocity
α_n^m	=	Inflow State Variables
δ_n^m	=	Inflow Co-state Variables
χ	=	Skew Angle of the Streamline
Ω	=	Rotor Speed
κ	=	Condition Number
$\bar{\lambda}$	=	Second Viscosity Coefficient

$\bar{\mu}$ = Dynamic Viscosity Coefficient

Φ = Pressure Potential of the Fluid

$\bar{\varphi}$ = Viscous Dissipation Function

Ψ_n^m = Prime Velocity Potentials (State-Space)

$\hat{\Psi}_n^m$ = Derived Velocity Potentials (State-Space)

ρ = Density of the Fluid

$\vec{\zeta}$ = Unit Vector Along the Streamline of the Flow

$\bar{\zeta}$ = Nondimensional Vector Along Streamline of the Flow

τ_n^m = Pressure Coefficient

θ = Velocity Potential of the Fluid

Acknowledgements

The work presented in this paper was partially funded through the U.S. Army/Navy/NASA Vertical Lift Research Center of Excellence at Georgia Tech under the direction of Mahendra Bhagwat of the US Army Futures Comment, Agreement No. W911W6-21-2-0001. Opinions, interpretations, conclusions, and recommendations are those of the authors and are not necessarily endorsed by the United States Government. This paper was prepared under the direction of David A. Peters.

Additionally, I would personally like to thank Dr. David A. Peters for his continued perseverance in guiding me along this research path, as well as the Washington University Chancellor's Fellowship and the McKelvey School of Engineering for their assistance and funding.

I would also like to thank Cory Seidel, Ph.D. for his assistance in MATLAB coding.

Michael Morrow

Washington University in St. Louis

May 2024

ABSTRACT OF THE DISSERTATION

Application of Finite-State Wake Models to

Rotors Re-entering Their Own Wake

by

Michael Morrow

Doctor of Philosophy in Mechanical Engineering

Washington University in St. Louis, 2024

Professor David A. Peters, Chair

This paper details the development of a finite-state, dynamic wake model for the purpose of modeling a helicopter rotor reentering its own wake. This model stems directly from both the Peters-Morillo wake model to determine the velocity field on and above the helicopter rotor and the Peters-Fei model to compute the velocity field below the rotor. The specific case of nonzero net thrust was evaluated under assumptions of axial flow and potential flow theory. Results consist of computations of the inflow velocity for this case, along with comparison to closed-form, potential flow solutions for validation. The finite-state model is shown to converge with the closed-form solutions up to 10 states prior to increasing divergence with an increasing number of states.

Chapter 1: Introduction

1.1 Research Motivation

Today, helicopter flight simulation programs are extremely important in the development of both current and future pilots, due to the variety of benefits simulation offer over direct machine usage (ease of access and cost, pilot and equipment safety, etc.). Simulation codes often include finite-state dynamic wake models that allow modeling of many aerodynamic interactions in real time. However, this type of modeling currently cannot accurately simulate the case in which a helicopter reenters its own wake (for example, when a helicopter is in hover or climb, then descends into its own wake). This is due to present finite-state wake modes only being able to handle the induced flow from the shed wake behind the helicopter. When the flow rate V is reversed to allow the wake to come back through the rotor, the finite-state equations become unstable because the induced flow from the wake is now growing rather than decaying.

Previous work with inflow models that preceded this paper began with the Pitt-Peters model [3], which developed an unsteady dynamic theory for helicopter rotor systems based on Mangler's actuator-disc theory. This model describes a perturbed induced inflow and pressure distribution in terms of ellipsoidal coordinates and the Legendre functions of the first and second kind.

However, Peters and Pitt were only able to obtain a preliminary wake description of uniform flow due to the fact that they only had first harmonics and no more than two radial shape functions. Improved accuracy of the model was realized through development of a higher harmonic theory by Peters and He [4]. Specifically, the Peters-He model extended the pressure distribution to include higher harmonic terms and an arbitrary number of radial functions for

each harmonic. The model assumes a superposition of pressure and excludes inflow models with no induced velocity on the disc, with concurrent results validated by wind tunnel data.

Later research into improvement into dynamic wake modeling saw Peters and Cao [5] look to find flow off the rotor disc in addition to and on the disc. They determined that a second set of wake states must exist for flow away from the disc, but they were unable to determine these states. Fortunately, Peters and Morillo [6] discovered that this second set could be solved rigorously without the need for the assumption of superposition of pressures from the Pitt-Peters model. This development was augmented by Hsieh [7] who added the singular potentials not found in [6]. Overall, Peters, Morillo, and Hsieh were able to solve for the velocity potential on the rotor disc and the velocity field anywhere above the disc. This gave all three components of velocity due to pressure across the disk or mass sources on the disk.

Peters and Fei [8] then completed the solution for the velocity field around the rotor disc by determining the induced flow below the rotor disc (including within the rotor wake), by use of the adjoint theorem, in which the adjoint states must be solved by time-marching in backward time in order to find the flow below the disk. These models do allow the flow freestream to vary during the simulation, but it is not allowed to reverse. When the freestream was changed to attempt reversal, it only sheds new vorticity into the new trailing wake and does not allow for reentry into the existing wake.

The primary purpose of this work is to use 3D dynamic wake modeling to first simulate the inflow case of a helicopter in climb/hover, then apply the same model to the helicopter descending and reentering back into its wake. This work is a direct addition to that of the Peters-Fei model (which is an addition onto the Peters-Morillo model). Closed-form equations of inflow pressure and velocity will be found for the simple case of nonzero net thrust, and these will then

be used to compare with dynamic modeling. The purpose is to then develop modifications to dynamic inflow to allow rotor reentry into the wake and then compare with the closed-form results.

1.2 Research Approach

The initial part of the work was to solve closed-form solutions to inflow pressure and velocity about the centerline of the helicopter rotor, beginning with the Potential Flow equations. From these equations, the pressure throughout the flow field surrounding the rotor is solved as a summation of the product of normalized Legendre functions of the 1^{st} and 2^{nd} kinds — and a general sinusoidal solution. This distribution corresponds to the simplest pressure of the Peters-He dynamic wake model. The pressure is then evaluated for the case of positive net thrust, thereby resulting in a specific closed-form solution. This is followed by finding the solution for inflow velocity for the same case. Unlike the resultant inflow pressure, the inflow velocity is dependent on time and the freestream velocity. To allow for the wake to reverse back into the rotor at a given time, a negative freestream velocity is applied to the inflow velocity solution.

The second part of the work involves coding the finite-state dynamic wake model for this simplest case of positive net thrust. Unlike the previously mentioned method, finite-state wake modeling does not result in an exact solution. Rather, it gives an approximate solution for inflow pressures and velocities based on a Galerkin approach. In theory, as more and more states are included in the Galerkin expansion, the solution will converge to the exact solution.

Chapter 2: Potential Flow Solutions in Closed-Form

2.1 Fluid Dynamics Equations

Within this work, a rotor disc is surrounded by a Newtonian fluid which is governed by the laws of conservation of mass, conservation of momentum, and conservation of energy. Additionally, the no-slip boundary condition at the solid-fluid interface of the rotor and fluid is in effect [2]. The conservation of mass is given as

$$\frac{\partial \rho}{\partial t} + \vec{\nabla} \cdot (\rho \vec{v}_t) = 0 \tag{2.1}$$

where ρ is the fluid density and $\vec{v}_t$ is the total velocity vector of the fluid. It is assumed that the helicopter is flying at standard atmospheric conditions, thereby resulting in the flow to be inviscid and incompressible. Equation (2.1) then reduces to

$$\vec{\nabla} \cdot \vec{v}_t = 0 \tag{2.2}$$

The conservation of momentum, described by the Navier-Stokes equations, for a viscous fluid is

$$\rho\left(\frac{\partial \vec{v}_t}{\partial t} + \vec{v}_t \cdot \vec{\nabla}\vec{v}_t\right) = -\vec{\nabla}p + \vec{\nabla}\left(\bar{\lambda}\,\vec{\nabla} \cdot \vec{v}_t\right) + \bar{\mu}\left[\vec{\nabla}\left(\vec{\nabla} \cdot \vec{v}_t\right) + \left(\vec{\nabla} \cdot \vec{\nabla}\right)\vec{v}_t\right] + \rho\vec{f} \tag{2.3}$$

where p is the pressure, $\bar{\lambda}$ is the second viscosity coefficient, $\bar{\mu}$ is the dynamic viscosity coefficient, and $\vec{f}$ represents external forces. Since the flow is assumed to be incompressible and inviscid, and assuming there are no significant body forces on the disc, equation (2.3) reduces to

$$\rho\left(\frac{\partial \vec{v}_t}{\partial t} + \vec{v}_t \cdot \vec{\nabla}\vec{v}_t\right) = -\vec{\nabla}p \tag{2.4}$$

Lastly, the conservation of energy can be expressed as

$$\rho\left(\frac{\partial e}{\partial t} + \vec{v}_t \cdot \vec{\nabla}e\right) = -\vec{\nabla}p \cdot \vec{v}_t + \vec{\nabla}\left(k\vec{\nabla}T\right) + \bar{\varphi} \tag{2.5}$$

where e is the internal energy per unit mass, k is the thermal conductivity of the fluid, T is the fluid temperature, and $\bar{\varphi}$ is the viscous dissipation function. Given that ρ and $\bar{\mu}$ are constant, the conservation of mass and momentum equations become uncoupled from the conservation of energy equation. Assuming adiabatic flow, the energy equation can be neglected. For this work, the velocity is considered to be a linearized equation:

$$\vec{v}_t = V_\infty \vec{\zeta} + \delta\vec{v} \tag{2.6}$$

where $\vec{\zeta}$ is a unit vector along the streamline of the flow, V_∞ is the steady freestream velocity, and the perturbation velocity, $\delta\vec{v}$, is defined as

$$\delta\vec{v} = \delta\vec{v}_x\vec{\imath} + \delta\vec{v}_y\vec{\jmath} + \delta\vec{v}_z\vec{k} \tag{2.7}$$

From Figure 2.1, the skew angle, χ, of the streamline is measured with respect to the positive z-axis such that

$$\vec{\zeta} = -\sin(\chi)\vec{\imath} + \cos(\chi)\vec{k} \tag{2.8}$$

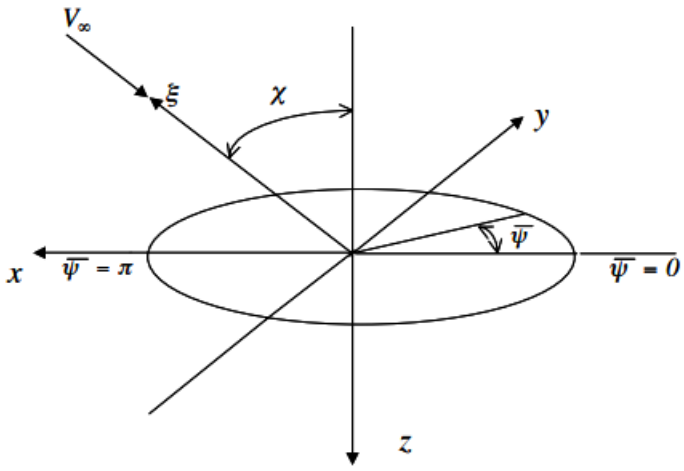

Figure 2.1. Streamline Coordinate System

The vectors $\vec{\imath}$, $\vec{\jmath}$, and $\vec{k}$ are in the x, y, and z directions, respectively. By substituting equation (2.6) into equations (2.2) and (2.4), while assuming V_∞ is constant:

$$\vec{\nabla} \cdot \delta\vec{v} = 0 \tag{2.9}$$

$$\rho \frac{\partial \delta\vec{v}}{\partial t} + \rho V_\infty \frac{\partial \delta\vec{v}}{\partial \zeta} = -\vec{\nabla} p \tag{2.10}$$

Nondimensionalization of all variables for length and velocity are done using the length scale of the rotor radius, *R*, the velocity scale, *ΩR*, and the mass scale associated with density, ρ. Additionally, the component of time is also nondimensionalized as $\bar{t} = \Omega t$. The Laplacian operator $\vec{\nabla}$ is redefined to represent the gradient with respect to the nondimensional coordinates. This nondimensionalization then leads to equations (2.9) and (2.10) to be

$$\vec{\nabla} \cdot \vec{v} = 0 \tag{2.11}$$

$$\frac{\partial \vec{v}}{\partial \bar{t}} + V \frac{\partial \vec{v}}{\partial \bar{\zeta}} = -\vec{\nabla} P \tag{2.12}$$

where $\vec{v} = \delta\vec{v}/\Omega R$, $V = V_\infty / \Omega R$, $\bar{\zeta} = \zeta / R$, and $P = p/\rho\Omega^2 R^2$.

2.2 Determination of Coordinate System

To begin the derivations of the inflow pressure and velocity distributions, an ellipsoidal coordinate system is chosen to allow the rotor disc to have a discontinuity in pressure across it. The pressure field in this coordinate system can then be used to find the surrounding velocity field. The rotor disk is therefore located at the discontinuity at η = 0. The discontinuity in the coordinate *v* across the rotor allows a pressure discontinuity to model the rotor disc. It follows that the rotor centerline becomes the case of *v* = 1 above the rotor and *v* = -1 below the rotor.

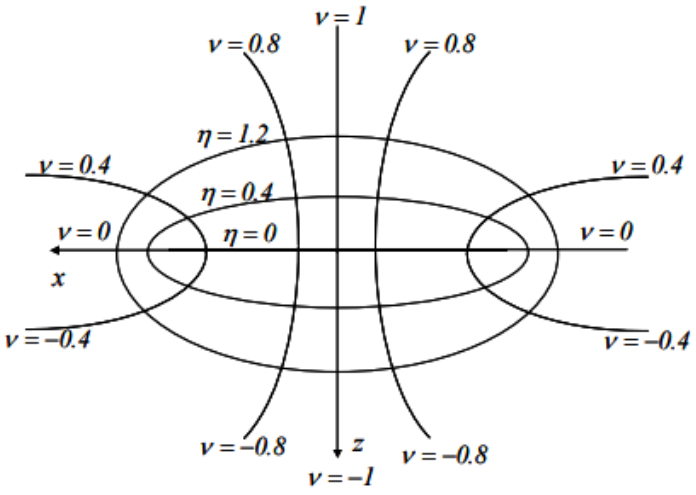

Figure 2.2. Ellipsoidal Coordinate System

$$x = -\sqrt{1-\nu^2}\sqrt{1+\eta^2}\cos\Psi$$

$$y = \sqrt{1-\nu^2}\sqrt{1+\eta^2}\sin\Psi \tag{2.13}$$

$$z = -\nu\eta$$

2.3 Pressure and Velocity Potentials

As this work focuses on the case of axial flow, the skew angle χ is therefore zero, and the streamline is along the *z*-axis. Consequently, equation (2.12) becomes

$$\frac{\partial\vec{v}}{\partial\bar{t}} + V\frac{\partial\vec{v}}{\partial z} = -\vec{\nabla}P \tag{2.14}$$

Assign *v* to be the gradient of a velocity potential *θ*. Then, then equations (2.11) and (2.14) become

$$\vec{v} = \vec{\nabla}\theta \tag{2.15}$$

$$\vec{\nabla}.\vec{v} = \vec{\nabla}.\vec{\nabla}\theta = 0 \tag{2.16}$$

$$\frac{\partial(\vec{\nabla}\theta)}{\partial\bar{t}} + V\frac{\partial(\vec{\nabla}\theta)}{dz} = -\vec{\nabla}P \tag{2.17}$$

By defining Φ as equal to P and applying the divergence operation (equation (2.19a)) on the updated momentum equation, Φ satisfies Laplace's equation, as seen in equation (2.19b) below. Additionally, Φ may also be defined as the pressure potential of the system.

$$\Phi = P \tag{2.18}$$

$$\frac{\partial(\vec{\nabla}.\vec{\nabla}\theta)}{\partial t} + V\frac{\partial(\vec{\nabla}.\vec{\nabla}\theta)}{dz} = -\vec{\nabla}.\vec{\nabla}\Phi \tag{2.19a}$$

$$\vec{\nabla}.\vec{\nabla}\Phi = \vec{\nabla}^2\Phi = 0 \tag{2.19b}$$

Laplace's equation in ellipsoidal coordinates then takes the following form:

$$\frac{\partial}{\partial\nu}\left[(1-\nu^2)\frac{\partial\Phi}{\partial\nu}\right] + \frac{\partial}{\partial\eta}\left[(1+\eta^2)\frac{\partial\Phi}{\partial\eta}\right] + \frac{\partial}{\partial\Psi}\left[\frac{(\nu^2+\eta^2)}{(1-\nu^2)(1+\eta^2)}\frac{\partial\Phi}{\partial\Psi}\right] = 0 \tag{2.20}$$

To solve equation (2.20), separation of variables is used to rewrite the equation as three separate equations, with each one corresponding to one of the three ellipsoidal coordinates ν, η, and Ψ:

$$\frac{\partial^2\Phi_3}{\partial\Psi^2} + m^2\Phi_3 = 0 \tag{2.21a}$$

$$\frac{\partial}{\partial\nu}\left[(1-\nu^2)\frac{\partial\Phi_1}{\partial\nu}\right] + \left[-\frac{m^2}{1-\nu^2} + n(n+1)\right]\Phi_1 = 0 \tag{2.21b}$$

$$\frac{\partial}{\partial\eta}\left[(1+\eta^2)\frac{\partial\Phi_2}{\partial\nu}\right] + \left[\frac{m^2}{1+\eta^2} - n(n+1)\right]\Phi_2 = 0 \tag{2.21c}$$

where m and n are constants of separation. The resultant pressure potential, Φ, is then the product of the solutions to equations (2.21a-c):

$$\Phi = \Phi(\nu,\eta,\Psi) = \Phi_1(\nu)\Phi_2(\eta)\Phi_3(\Psi) \tag{2.22}$$

The resulting pressure distribution is shown below:

$$\Phi = P(\nu, \eta, \Psi) = -\frac{1}{2}\sum_{m=0}^{\infty}\sum_{n=m+1}^{\infty} \bar{P}_n^m(\nu)\ \bar{Q}_n^m(i\eta)[\tau_n^{mc}cos(m\Psi) + \tau_n^{ms}sin(m\Psi)] \quad (2.23)$$

where $\bar{P}_n^m(\nu)$ and $\bar{Q}_n^m(i\eta)$ are the normalized Legendre functions of the first and second kind, and m takes value from 0, 1, 2, …,∞, and n is from m+1, m+2, …, ∞. The sine and cosine terms of the pressure potential in equation (2.23) can be composed as

$$\Phi_n^{mc}(\nu, \eta, \Psi) = \bar{P}_n^m(\nu)\ \bar{Q}_n^m(i\eta)cos(m\Psi) \quad (2.24)$$

$$\Phi_n^{ms}(\nu, \eta, \Psi) = \bar{P}_n^m(\nu)\bar{Q}_n^m(i\eta)sin(m\Psi) \quad (2.25)$$

For the net thrust case, m = 0 and n = 1 only; thus, the net thrust pressure distribution is

$$P = -\frac{1}{2}\bar{P}_1^0(\nu)\bar{Q}_1^0(i\eta)[\tau_1^0 cos(0)]$$

$$P = -\frac{\sqrt{3}\nu}{2}\left[1 - \eta * tan^{-1}\left(\frac{1}{\eta}\right)\right]\tau_1^0 \quad (2.26)$$

where τ_1^0 is a step function of the pressure. To ensure a unity maximum pressure magnitude at the rotor disc (η = 0), let τ_1^0 equal

$$\tau_1^0 = \frac{2}{\sqrt{3}}$$

Finally, by substituting z for η (along the centerline where ν equals either -1 for $z > 0$ or 1 for $z < 0$), the pressure P is now

$$P = -\nu\left[1 - z * tan^{-1}\left(\frac{1}{z}\right)\right] \quad (2.27)$$

or

$$P = \begin{cases} -1 + z * tan^{-1}\left(\frac{1}{z}\right), & z < 0 \\ 1 - z * tan^{-1}\left(\frac{1}{z}\right), & z > 0 \end{cases} \quad (2.28)$$

2.4 Evolving Wake Velocity Distribution

After determining the pressure distribution, the velocity distribution *v* can now be found by solving for both the particular solution, $\vec{v}_p$, and homogeneous solution, $\vec{v}_h$, of equation (2.14):

$$V\frac{\partial \vec{v}_p}{dz} = -\frac{\partial P}{\partial z} \tag{2.29}$$

$$\frac{\partial \vec{v}_h}{d\bar{t}} + V\frac{\partial \vec{v}_h}{dz} = 0 \tag{2.30}$$

The resulting solutions for $\vec{v}_p$ and $\vec{v}_h$ are as follows:

$$\vec{v}_p(z) = \begin{cases} \frac{1}{V}\left[1 - z * tan^{-1}\left(\frac{1}{z}\right)\right], & z < 0 \\ \frac{1}{V}\left[1 + z * tan^{-1}\left(\frac{1}{z}\right)\right], & z > 0 \end{cases} \tag{2.31}$$

$$\vec{v}_h(z,\bar{t}) = \begin{cases} -\frac{1}{V}\left[1 - (z - V\bar{t}) * tan^{-1}\left(\frac{1}{z - V\bar{t}}\right)\right], & z - V\bar{t} < 0 \\ -\frac{1}{V}\left[1 + (z - V\bar{t}) * tan^{-1}\left(\frac{1}{z - V\bar{t}}\right)\right], & z - V\bar{t} > 0 \end{cases} \tag{2.32}$$

The velocity distribution of the flow is therefore the summation of the particular and homogeneous solutions:

$$\vec{v}(z,\bar{t}) = \begin{cases} \frac{1}{V}\left[(z - V\bar{t})\tan^{-1}\left(\frac{1}{z - V\bar{t}}\right) - z\tan^{-1}\left(\frac{1}{z}\right)\right], & z < 0,\ \ \bar{t} > 0 \\ \frac{1}{V}\left[(z - V\bar{t})\tan^{-1}\left(\frac{1}{z - V\bar{t}}\right) + z\tan^{-1}\left(\frac{1}{z}\right)\right], & 0 < z < V\bar{t},\ \ \bar{t} > 0 \\ \frac{1}{V}\left[z\tan^{-1}\left(\frac{1}{z}\right) - (z - V\bar{t})\tan^{-1}\left(\frac{1}{z - V\bar{t}}\right)\right], & z > V\bar{t},\ \ \bar{t} > 0 \end{cases} \tag{2.33}$$

Plotting the above equation for the inflow velocity versus the distance perpendicular to the rotor disc along the centerline, *z*, over time will show the velocity present at the rotor disc to approach *V* and the maximum velocity downstream to approach 2*V*. The same plot is also a good

representation of the wake caused by the rotor, which grows further downstream as time progresses.

2.5 Wake Reversal via Closed-Form Solutions

A modification to equation (2.33) can be made to allow the wake at a given time t_{stop} to translate downstream and later reverse its direction to move back into the rotor disc as opposed to continue to grow. This simulates the act of the helicopter transitioning from climb to descent and the new wake, thus intermixing with the previous wake generated through climbing. The first change is to apply a sinusoidal transition of the freestream velocity V from +1 to -1 over a time π/k, thereby also making V time-dependent:

$$V(\bar{t}) = \begin{cases} 1, & \bar{t}_{stop} < \bar{t} < \bar{t}_0 \\ \cos[k(\bar{t} - t_0)], & \bar{t}_0 < \bar{t} < \bar{t}_o + \dfrac{\pi}{k} \\ -1, & \bar{t} > \bar{t}_o + \dfrac{\pi}{k} \end{cases} \tag{2.34}$$

Given the freestream velocity is now a function of time, the distance the wake propagates can be found by taking the integral of $V(\bar{t})$ with respect to time (this distance was initially $V^*\bar{t}$ in Eq. 24 for the case of constant $V(\bar{t})$:

$$s(\bar{t}) = \int_{\bar{t}_{stop}}^{\bar{t}} V(\bar{t})\, \mathrm{d}\bar{t}$$

$$s(\bar{t}) = \begin{cases} \bar{t} - \bar{t}_{stop}, & \bar{t}_{stop} < \bar{t} < \bar{t}_0 \\ \dfrac{1}{k}\sin[k(\bar{t} - \bar{t}_0)] + (\bar{t} - \bar{t}_{stop}), & \bar{t}_0 < \bar{t} < \bar{t}_o + \dfrac{\pi}{k} \\ 2t_0 - \bar{t}_{stop} + \dfrac{\pi}{k} - \bar{t}, & \bar{t} > \bar{t}_o + \dfrac{\pi}{k} \end{cases} \tag{2.35}$$

Replacing the $V^*\bar{t}$ terms with $s(\bar{t})$ in equation (2.33) results in

$$\vec{v}(z,\bar{t}) = \begin{cases} (z - s(\bar{t}))\tan^{-1}\left(\dfrac{1}{z - s(\bar{t})}\right) - z\tan^{-1}\left(\dfrac{1}{z}\right), & z < 0,\ \ \bar{t} > \bar{t}_{stop} \\ (z - s(\bar{t}))\tan^{-1}\left(\dfrac{1}{z - s(\bar{t})}\right) + z\tan^{-1}\left(\dfrac{1}{z}\right), & 0 < z < s(\bar{t}),\ \ \bar{t} > \bar{t}_{stop} \\ z\tan^{-1}\left(\dfrac{1}{z}\right) - \left(z - s(\bar{t})\right)\tan^{-1}\left(\dfrac{1}{z - s(\bar{t})}\right), & z > s(\bar{t}),\ \ \bar{t} > \bar{t}_{stop} \end{cases} \quad (2.36)$$

To simplify equation (2.36), let $n(z, \bar{t})$ denote the difference between z and $s(\bar{t})$:

$$n = n(z,\bar{t}) = z - s(\bar{t})$$

$$n(z,\bar{t}) = \begin{cases} z - (\bar{t} - \bar{t}_{stop}), & \bar{t}_{stop} < \bar{t} < \bar{t}_0 \\ z - \left\{\dfrac{1}{k}\sin[k(\bar{t} - \bar{t}_0)] + (\bar{t}_0 - \bar{t}_{stop})\right\}, & \bar{t}_0 < \bar{t} < \bar{t}_0 + \dfrac{\pi}{k} \\ z - \left(2\bar{t}_0 - \bar{t}_{stop} + \dfrac{\pi}{k} - \bar{t}\right), & \bar{t} > \bar{t}_0 + \dfrac{\pi}{k} \end{cases} \quad (2.37)$$

Then, the velocity distribution of the wake after time $\bar{t}_{stop}$ becomes

$$\vec{v}(z,\bar{t}) = \begin{cases} \left(n - \bar{t}_{stop}\right)\tan^{-1}\left(\dfrac{1}{n - \bar{t}_{stop}}\right) - n\tan^{-1}\left(\dfrac{1}{n}\right), & n < 0,\ \ \bar{t} > \bar{t}_{stop} \\ \left(n - \bar{t}_{stop}\right)\tan^{-1}\left(\dfrac{1}{n - \bar{t}_{stop}}\right) + n\tan^{-1}\left(\dfrac{1}{n}\right), & 0 < n < \bar{t}_{stop},\ \ \bar{t} > \bar{t}_{stop} \\ n\tan^{-1}\left(\dfrac{1}{n}\right) - \left(n - \bar{t}_{stop}\right)\tan^{-1}\left(\dfrac{1}{n - \bar{t}_{stop}}\right), & n > \bar{t}_{stop},\ \ \bar{t} > \bar{t}_{stop} \end{cases} \quad (2.38)$$

Notice that equations (2.33) and (2.38) bear a striking resemblance to one another; the transformation of z to n is completely equivalent with the applied transformation of $\bar{t}$ to $\bar{t}_{stop}$ as the reference time. This is because the homogeneous solution of the velocity — as defined by Eq. (2.14) — is any function of $(z - V\bar{t})$. Thus, z and $V\bar{t}$ always appear in parallel for the homogeneous solution for the velocity distribution.

Therefore, for any time prior to $\bar{t}_{stop}$, the wake velocity will follow the growth distribution described in equation (2.33), then follow the translation distribution described in equation (2.38) after time $\bar{t}_{stop}$. Note that this translation of the wake can be altered to either be strictly

downstream, reverse direction and begin to travel upstream back towards the rotor, or anything in between by changing the nature of $V(\bar{t})$.

2.6 Results from the Closed-Form Solutions

The following figure shows the pressure distribution across the rotor disc. It can be seen that the far-field upstream ($z < 0$) pressure approaches zero, coinciding with the atmospheric pressure of the ambient air. The pressure upstream of the disc then becomes increasingly negative, reaching a maximum in magnitude at the disc ($z = 0$). A pressure discontinuity then occurs at the rotor disc as the pressure jumps from negative to positive, with the magnitude remaining constant. Increasingly downstream of the rotor ($z > 0$), the pressure then decreases to zero.

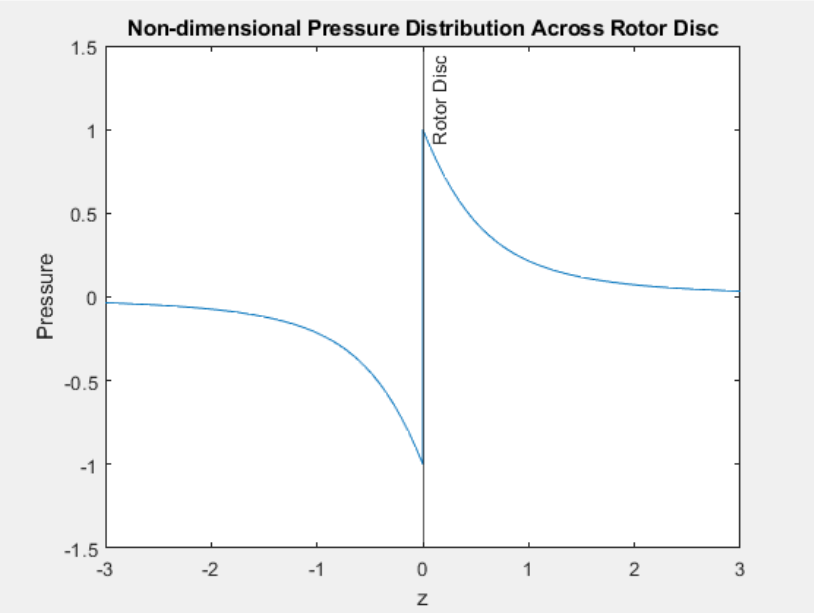

Figure 2.3. Closed-Form Pressure Distribution

This result is consistent with the process in how helicopters use their main rotors to create lift by pulling in air above the rotor and pushing the same air beneath the rotor, thereby lifting itself upwards in accordance with Newton's third law of motion.

Given the velocity distribution is not only a function of length z but also time t, plotting the velocity along the centerline of the rotor disc will change over time, either with the growth of the wake downstream as in equation (2.23) or the translation of a wake of constant size correspondent to equation (2.38). The following figures follow a specific process of the velocity in which the rotor disc "turns on" at $\bar{t} = 0$ and "shuts off" at $\bar{t} = 5$ (time step = 0.1). The red line labelled "Time" is indicative of both the current time $\bar{t}$ as well as the end of the wake generated by the rotor disc. After this, the rotor disc will "descend" causing the previously impacted air to interact with the disc. Note that the frequency k present within equation (2.38) via the distribution n equals $\pi/5$.

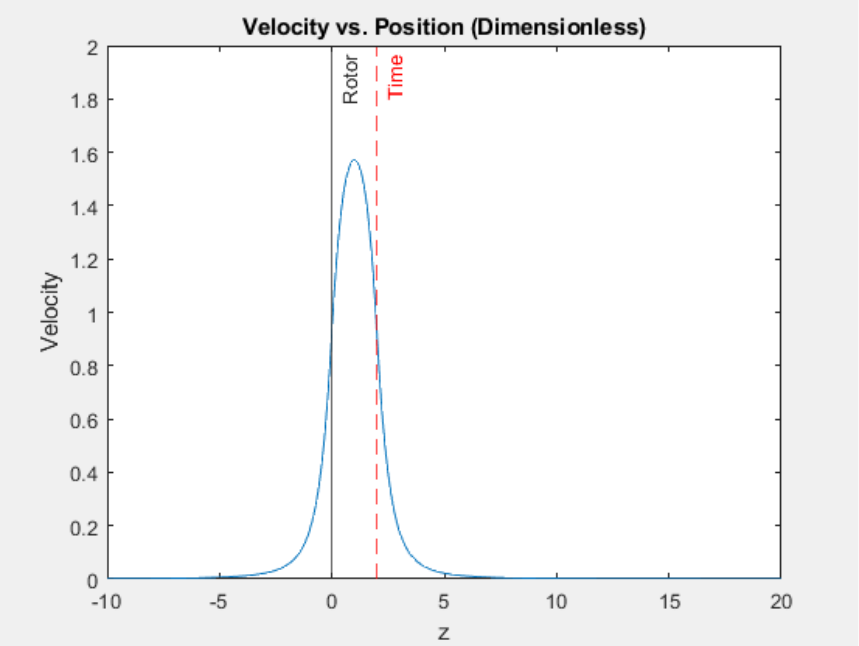

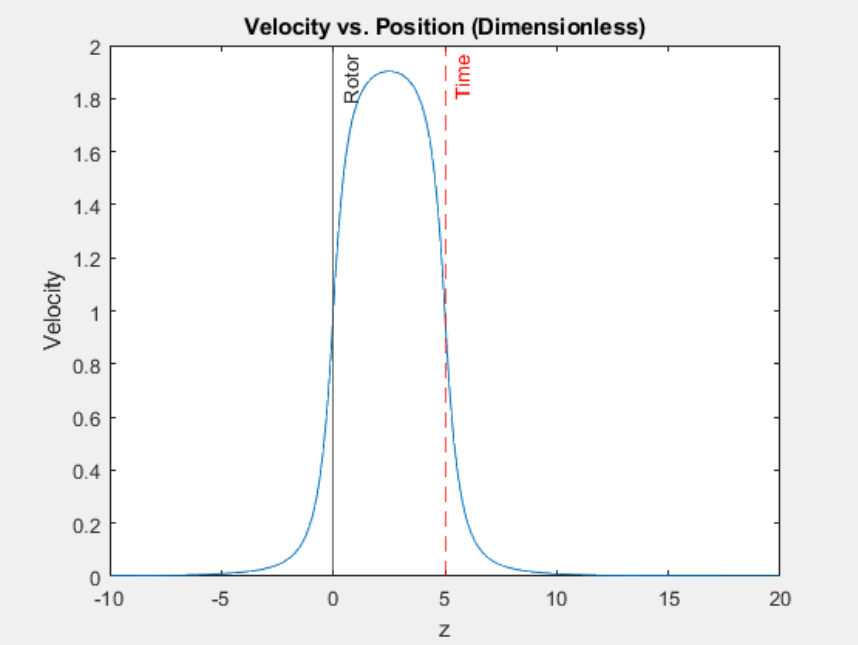
Velocity vs. Position (Dimensionless)
Rotor
Time
Velocity
z
2
1.8
1.6
1.4
1.2
1
0.8
0.6
0.4
0.2
0
-10
-5
0
5
10
15
20

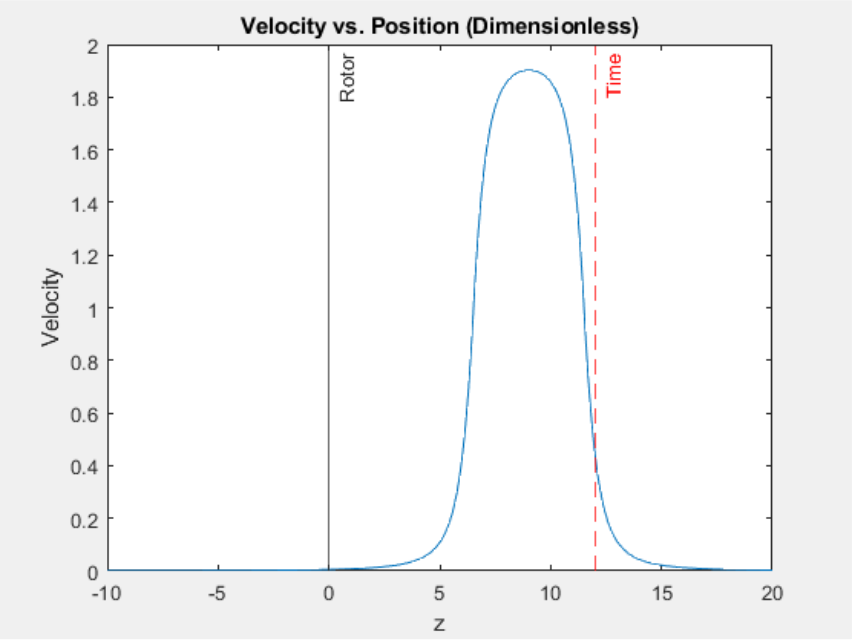
Velocity vs. Position (Dimensionless)
Rotor
Time
Velocity
z
2
1.8
1.6
1.4
1.2
1
0.8
0.6
0.4
0.2
0
-10
-5
0
5
10
15
20

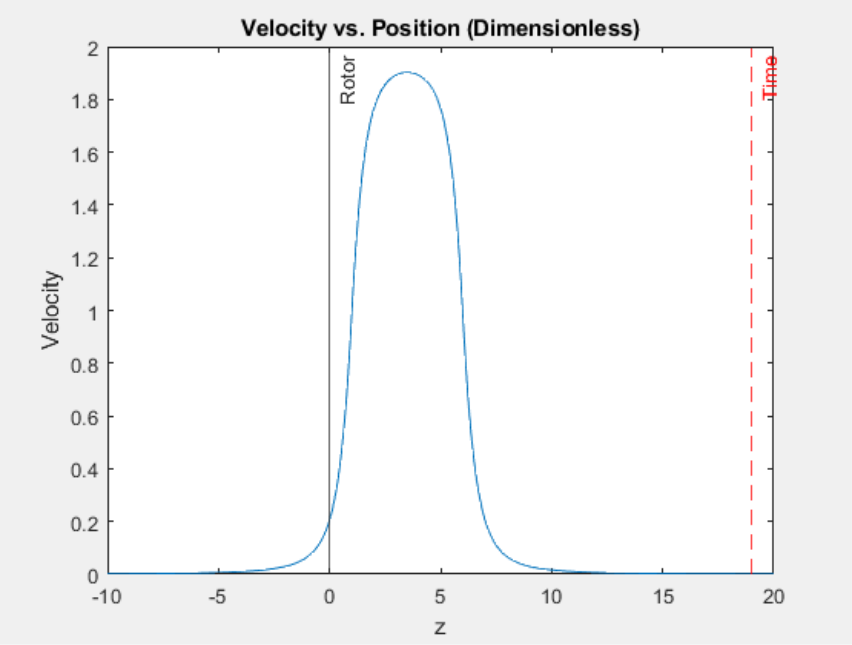

Figure 2.4 a-d. Velocity Distribution: Growth, Translation, and Reversal

An interesting observation is seen when looking at the ratio between the maximum induced velocity occurring downstream and the velocity at the rotor at a given time. As can be seen in Figure 2.4, the velocity of the air at the rotor begins to increase as the rotor is in operation. Over time, this rotor velocity continues to increase until approximately reaching a maximum value of 1. During this process, the velocity downstream also increases to a value exceeding that at the rotor. Specifically, the maximum velocity at any point downstream is equal to roughly twice the velocity concurrent with the rotor, a result consistent with momentum theory. In addition, if the rotor stays operational for an extended period of time, following the distribution outlined in equation (2.33), then the velocity at the majority of the locations downstream will approach twice the velocity at the rotor disc, as seen in Figure 2.5.

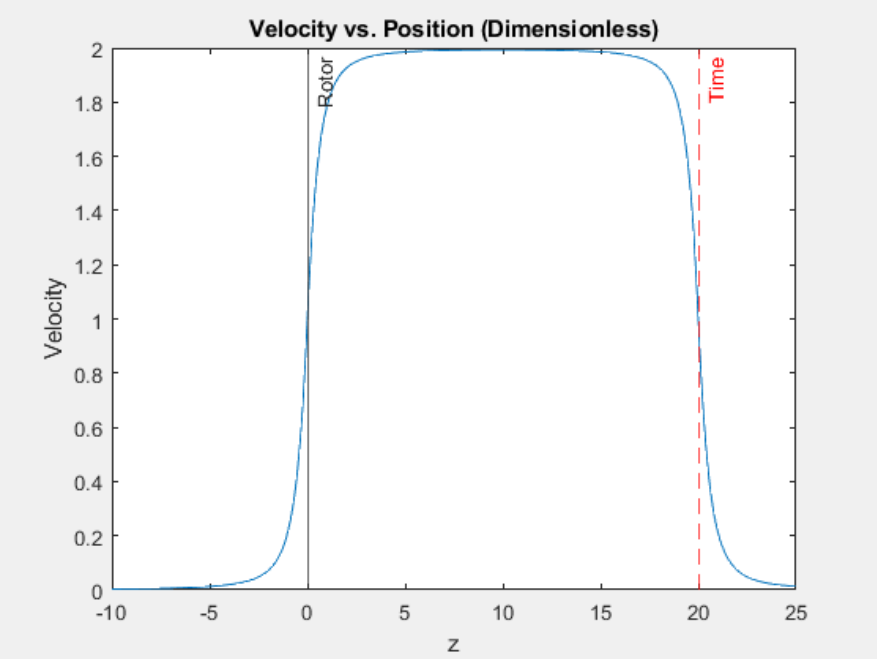

Figure 2.5. Continuously Growing Wake (Helicopter In Climb)

Chapter 3: State-Space Approach

3.1 Method of Weighted Residuals: Galerkin Method

To convert the partial differential equations (2.11) and (2.12) into matrix form for finite-state numerical analysis, Morillo elected to use the method of weighted residuals [6] which allows one to find an approximate solution, u_a, to a differential equation:

$$L(u) = 0 \tag{3.1}$$

on the domain $D(\vec{x})$, subject to initial conditions $I(u) = 0$ and boundary conditions $S(u) = 0$ on ∂D, the boundary of *D*. The approximate solution can be structured such that the differential equation is wholly satisfied (boundary method), the boundary conditions are wholly satisfied (interior method), or neither the differential equation nor the boundary conditions are wholly satisfied (mixed method).

Using the method of weighted residuals, the approximate solution, u_a, is written as a set of known analytic functions called trial functions, $\phi(\vec{x})$:

$$u_a(\vec{x}, t) = \sum_{j=1}^{N} a_j(t)\phi_j(\vec{x}) \tag{3.2}$$

where the coefficients a_j must be determined. By substituting equation (3.2) into equation (3.1), a differential equation for a_j is obtained. In addition, since equation (3.2) is an approximate solution, a nonzero residual, *R*, arises:

$$R(a_1, a_2, \dots, a_n, \vec{x}) = L(u_a) = \sum_{j=1}^{N} a_j L(\phi_j) \neq 0 \tag{3.3}$$

The equations for the coefficients a_j are obtained by multiplying the residuals, *R*, by weights or test functions, $\lambda_k(\vec{x})$, which are then integrated over domain *D* and set equal to zero:

$$\iint_D R\lambda_k(\vec{x})dD = 0; \quad k = 1,2,\ldots,N \tag{3.4}$$

Equation (3.4) is what gives the name to this methodology.

The Galerkin method is thus a specific case to the method of weighted residuals where the test functions are chosen to be the same set of functions as the trial functions:

$$\lambda_k(\vec{x}) = \phi_k(\vec{x}); \quad k = 1,2,\ldots,N \tag{3.5}$$

The following conditions are necessary to apply the Galerkin method and correctly choose the weight functions:

(1) ϕ and λ_k must be linearly independent sets of functions.

(2) ϕ and λ_k should be the first *N* members of a complete set of functions.

(3) ϕ should satisfy the boundary conditions (as well as initial conditions if applicable).

A "complete" set of functions suggests the functions satisfy Laplace's equation in the upper half plane of the flow field, are zero at infinity, and are finite on the rotor disc plane.

3.2 Pressure Potentials and Velocity Potentials

In order to transform equations (2.11) and (2.12) by the Galerkin method, the pressure potentials, Φ, and the velocity potentials, Ψ, must be expanded in terms of complete sets of that satisfy Laplace's equation. Both Φ and Ψ must also satisfy the boundary conditions for pressure and velocity, respectively.

The boundary conditions for pressure calls for a discontinuity across the rotor disc and zero pressure far away from the disc, the first of which is satisfied by the solution to Laplace's equation in ellipsoidal coordinates given that ν is discontinuous across $z = \eta = 0$. Equations (2.24) and (2.25) detail the solution to Laplace's equation:

$$\Phi_n^{mc}(\nu,\eta,\Psi) = \bar{P}_n^m(\nu)\,\bar{Q}_n^m(i\eta)cos(m\Psi) \tag{2.24}$$

$$\Phi_n^{ms}(\nu,\eta,\Psi) = \bar{P}_n^m(\nu)\,\bar{Q}_n^m(i\eta)sin(m\Psi) \tag{2.25}$$

where m = 0, 1, 2, …,∞, and n = m, m+1, m+2, …, ∞. Additionally, the pressure potentials, Φ_n^m, are zero in the far-field, given $\lim_{\eta\to\infty} \bar{Q}_n^m\,(i\eta) = 0$, satisfying the second boundary condition, and finite at z = 0. Therefore, the pressure expansion, P, can be defined as the summation of terms that include both the cosine and sine pressure coefficients, τ_n^{mc} and τ_n^{ms}, respectively:

$$P = -\sum_{m=0}^{\infty}\sum_{n=m}^{\infty}(\tau_n^{mc}\Phi_n^{mc} + \tau_n^{ms}\Phi_n^{ms}) \tag{3.6}$$

Previous work outlining finite-state modeling details two sets of velocity potentials, derived potentials, and prime potentials [2]. The boundary conditions for the velocity state that the velocity field far upstream relative to the rotor must equal zero. To satisfy this condition, prime velocity potentials are defined as [2]

$$\Psi_n^{mc} = \int_{-\infty}^{\zeta}\Phi_n^m\cos(m\bar{\Psi})d\zeta \tag{3.7}$$

$$\Psi_n^{ms} = \int_{-\infty}^{\zeta}\Phi_n^m\,sin(m\bar{\Psi})d\zeta \tag{3.8}$$

where m = 0, 1, 2, …,∞, and n = m+1, m+2, …, ∞. This stems from the fact that the pressure potentials, Φ_n^m, are zero far upstream, strongly ensuring the same result for Ψ_n^m. The flow velocities can then be represented as an expansion summation of the gradient of the prime potentials from equations (3.6) and (3.7):

$$\vec{v} = \sum_{m=0}^{\infty}\sum_{n=m}^{\infty}\left(\hat{a}_n^m\vec{\nabla}\Psi_n^{mc} + \hat{b}_n^m\vec{\nabla}\Psi_n^{ms}\right) \tag{3.10}$$

Note that $\hat{a}_n^m$ and $\hat{b}_n^m$ are the cosine and sine induced inflow expansion coefficients, respectively.

3.3 Derived Velocity Potentials

In order to modify the prime velocity potentials for axial flow, derived potentials, $\widehat{\Psi}_n^m$, are chosen in a way that their gradient can be written in closed form. Unlike the derived potentials, the prime potentials must be integrated along a streamline to determine the velocity, whereas the derived potentials avoid this numerical integration. That being said, the derived potentials are simply the prime potentials in the case of axial flow. These derived potentials are defined such that their derivative with respect to *z* is

$$\frac{d\widehat{\Psi}_n^{mc}}{dz} = \bar{P}_n^m(\nu)\, \bar{Q}_n^m(i\eta)\cos(m\bar{\Psi}) \tag{3.11}$$

$$\frac{d\widehat{\Psi}_n^{ms}}{dz} = \bar{P}_n^m(\nu)\, \bar{Q}_n^m(i\eta)sin(m\bar{\Psi}) \tag{3.12}$$

Peters and Morillo [6] found these derived potentials in the following form:

$$\widehat{\Psi}_n^m = \sigma_n^m \Phi_{n+1}^m + \zeta_n^m \Phi_{n-1}^m \tag{3.13}$$

where

$$\sigma_n^m = \frac{1}{K_n^m \sqrt{(2n+1)(2n+3)[(n+1)^2 - m^2]}} \tag{3.14}$$

$$\zeta_n^m = \frac{1}{K_n^m \sqrt{(4n^2-1)(n^2-m^2)}} \qquad n \neq m \tag{3.15}$$

and

$$K_n^m = \left(\frac{\pi}{2}\right)^{(-1)^{n+m}} H_n^m \tag{3.16}$$

$$H_n^m = \frac{(n+m+1)!!\,(n-m-1)!!}{(n+m)!!\,(n-m)!!} \tag{3.17}$$

The above definition of the derived potentials is only valid above the rotor disc ($z < 0$). Morillo was able to find the potentials for cases where $m \neq n$, while Peters and Hsieh were later able to find the potentials for the special cases of $m = n = 0$ and $m = n \neq 0$. For the case of $m = n =$

0, a formula in terms of the Legendre functions where the subscript is greater than the superscript was developed [7].

For $m = n = 0$:

$$\widehat{\Psi}_n^{mc} = [\sigma_n^m \bar{P}_{m+1}^m(\nu)\bar{Q}_{m+1}^m(i\eta) + \bar{P}_{m-1}^m(\nu)\bar{Q}_{m-1}^m(i\eta)]\cos(m\bar{\Psi}) \tag{3.18}$$

$$\widehat{\Psi}_n^{ms} = [\sigma_n^m \bar{P}_{m+1}^m(\nu)\bar{Q}_{m+1}^m(i\eta) + \bar{P}_{m-1}^m(\nu)\bar{Q}_{m-1}^m(i\eta)]\sin(m\bar{\Psi}) \tag{3.19}$$

Note that the "alternative" Legendre terms contain an *m-1* subscript. The determination for these necessary first and second Legendre functions are

$$\bar{P}_{m-1}^m(\nu) = \frac{2}{\pi}\frac{\sqrt{(2m)!!}}{\sqrt{(2m+1)!!}}\frac{(1-\nu^2)^{m/2}}{(1+\nu)^m}\sum_{n=0}^{m-1}\frac{(m-1)!\,2^{m-1-n}(-1)^n}{n!\,(m-1-n)!\,(n+m)}(1-\nu)^n \tag{3.20}$$

$$\bar{Q}_{m-1}^m(i\eta) = \frac{1}{(1+\eta^2)^{m/2}} \tag{3.21}$$

For the special case of $m = n = 0$, Peters and Hsieh found the derived potential to equal [7]

$$\widehat{\Psi}_0^0 = \frac{2}{\pi}\nu\left[1 - \eta\tan^{-1}\left(\frac{1}{\eta}\right)\right] - \frac{2}{\pi}ln|1+\nu| - \frac{1}{\pi}ln|1+\eta^2| + \frac{2}{\pi}ln|Z_{max}| \quad \nu > 0 \tag{3.22}$$

where Z_{max} is a large number representing the radius to which the integral with respect to ζ is taken. The value of Z_{max} is not entered in the equations; it is only a conceptual idea.

As the velocity potentials satisfy the Laplace equation, the continuity equation is satisfied as well. Therefore, the momentum equation is the only governing equation of the velocity expansion coefficients. The momentum equation must then be represented in finite state form in order to obtain a consequent finite-state wake model.

3.4 Equations in Terms of the Derived Potentials

To transform the momentum equation into a set of ordinary differential equations, the Galerkin method is applied (Appendix A). A change of variable is then needed to find the velocity via the derived potentials. The relationship to transform between the two potentials must obey the following:

$$\{\hat{\alpha}_n^m\}^T[\Psi_n^{mc}] = \{\alpha_n^m\}^T\left[\widehat{\Psi}_n^m\right] = \{\alpha_n^m\}^T\{\sigma_n^m\Phi_{n+1}^m + \zeta_n^m\Phi_{n-1}^m\} \tag{3.23}$$

where α_n^m is denoted as the inflow state variables. In order to find the transform between the two bases, the prime and derived potential functions are dotted with the gradient of each potential function and integrated over the region above the rotor disc [6]. The resulting relation between the potential types is

$$\{\hat{\alpha}_n^m\} = [\tilde{L}^c]^{-1}[M^c]\{\alpha_n^m\} \tag{3.24}$$

where

$$[\tilde{L}^c] = \left[\iint_s \frac{\partial\Phi_j^{rc}}{\partial z}\left(\int_0^\infty \Phi_n^{mc}\, d\zeta\right) ds\right] = \left[\iint_s \Phi_j^{rc}\frac{\partial}{\partial z}\left(\int_0^\infty \Phi_n^{mc}\, d\zeta\right) ds\right] \tag{3.25}$$

and

$$[M^c] = [\tilde{L}^c]_{\chi=0} = \left[\iint_s \frac{\delta\Phi_j^{rc}}{\delta z}\Psi_n^{mc}\, ds\right] \tag{3.26}$$

A similar relationship exists between $\{\hat{b}_n^m\}$ and $\{b_n^m\}$ that incorporates the $[L^s]$ and $[M^s]$ terms that relate the sine coefficients. With the appropriate change of variables realized, the momentum equation in terms of the derived potentials is found to be

$$[M^c]\{\dot{\alpha}_n^m\} + \boldsymbol{V}[D^c][\tilde{L}^c]^{-1}[M^c]\{\alpha_n^m\} = [D^c]\{\tau_n^{mc}\} \tag{3.27}$$

The above equation represents all the velocity components above and on the rotor plane in closed form. Equation (3.27) can be further reduced for the case of axial flow ($\chi = 0$) where $[M^c]$ and $[\tilde{L}^c]$ are equivalent. This simplified equation of motion is

$$[M^c]\{\dot{\alpha}_n^m\} + \boldsymbol{V}[D^c]\{\alpha_n^m\} = [D^c]\{\tau_n^{mc}\} \tag{3.28}$$

3.5 Velocity Below the Rotor Disc by the Adjoint Theorem

The aforementioned Galerkin integrals are limited to solutions to the velocity above and on the rotor disc due to the complex boundary conditions below the rotor plane [6]. Specifically, vortex shedding caused by the blades creates vortex sheets below the rotor, thereby invalidating the Potential Flow assumption (no longer irrotational) for the entire downstream flow field (this assumption still holds between the vortex sheets, however). That being said, the flow below the rotor disc still satisfies the conservation of mass and momentum equations, thus allowing for this flow to be obtained in terms of the flow field on and above the disc. This was the case for Zhongyang Fei's work with the adjoint theorem and adjoint states (or co-states) [8]. The adjoint theorem was a result from a closed-form solution for the frequency response below a perturbed disc, which then transformed into the time domain [2]. A complex conjugate within the frequency domain translated into an adjoint in the time domain. Time delays also appeared in the transformation to the time domain. The resultant solution for the velocity at a location ζ_0 below the rotor disc is

$$\vec{v}(r_0, \bar{\Psi}_0, \zeta_0, \bar{t}) = \vec{v}(r_0, \bar{\Psi}_0, 0, \bar{t} - \zeta_0) + \vec{v}^*(r_0, \bar{\Psi}_0, 0, \bar{t} - \zeta_0) - \vec{v}^*(r_0, \bar{\Psi}_0, -\zeta_0, \bar{t}) \tag{3.29}$$

where $\vec{v}^*$ is the adjoint velocity, $\bar{\Psi}_0$ is the adjoint azimuth angle, r_0 is the radial location of the intersection point of the streamline with the rotor plane, and $\bar{t} - \zeta_0$ is a time delayed term. Note

that the velocity solution in Eq. (3.29) does not include a jump in velocity across the rotor disc resulting from mass sources [2].

Looking at Eq. (3.29) and Figure 3.1, $\vec{v}(r_0, \bar{\Psi}_0, \zeta_0, \bar{t})$ is the velocity below the rotor disc at point a along the streamline; $\vec{v}(r_0, \bar{\Psi}_0, 0, \bar{t} - \zeta_0)$ is the velocity where the free streamline intersects the rotor plane at point b; $\vec{v}^*(r_0, \bar{\Psi}_0, 0, \bar{t} - \zeta_0)$ is the adjoint velocity at point c which is centrosymmetric to point b; $\vec{v}^*(r_0, \bar{\Psi}_0, -\zeta_0, \bar{t})$ is the adjoint velocity at point d above the rotor disc which is centrosymmetric to point a.

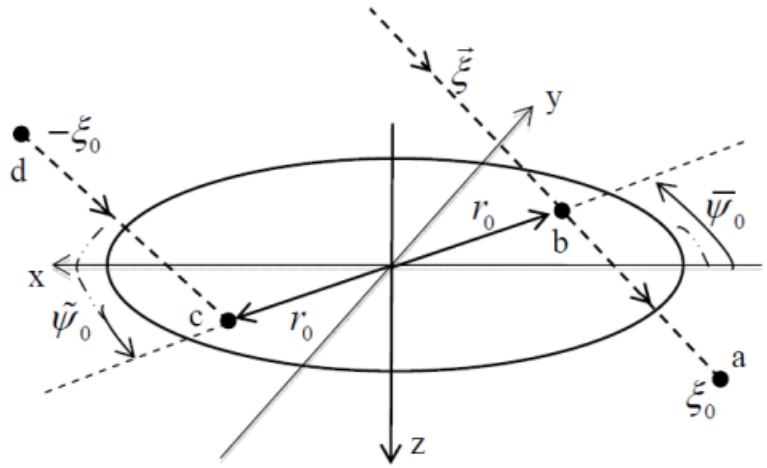

Figure 3.1. Rotor Disc with Velocity Components Used in Eq. (3.29)

The adjoint to the momentum equation is

$$-[M^c]\left\{\dot{\bar{\delta}}_n^m\right\} + \boldsymbol{V}[D^c][\tilde{L}^c]^{-1}[M^c]\{\bar{\delta}_n^m\} = [D^c]\begin{bmatrix} \ddots & & \\ & (-1)^{n+1} & \\ & & \ddots \end{bmatrix}\{\tau_n^{mc}\} \tag{3.30}$$

where δ_n^m is denoted as the inflow co-state variables. This equation must be solved backwards in time for the co-state variables, as the solution is unstable in forward time marching [2].

3.6 Velocity Solution for Single Lifting Rotor System in Axial Flow

For a single lifting rotor system, the velocity on and above the rotor disc is found using state variables, α_n^m, which is determined from

$$[M]\{\dot{\alpha}_n^m\} + \boldsymbol{V}[D][\tilde{L}]^{-1}[M]\{\alpha_n^m\} = [D]\{\tau_n^m\} \tag{3.31}$$

The velocity below the rotor disc is found using the adjoint theorem and determining the co-state variables, δ_n^m:

$$-[M]\{\dot{\delta}_n^m\} + \boldsymbol{V}[D][\tilde{L}]^{-1}[M]\{\delta_n^m\} = [D]\begin{bmatrix} \ddots & & \\ & (-1)^{n+1} & \\ & & \ddots \end{bmatrix}\{\tau_n^m\} \tag{3.32}$$

In these equations, [M] is the apparent mass matrix, [D] is the damping matrix, [L] is the influence coefficient matrix, and τ_n^m is the pressure coefficient. The processes for determining the mass, damping, and influence coefficient matrices are discussed in Appendix A. In axial flow, which is the case throughout this work, the relationship holds such that $[L] = [M]$. Simplifying and rearranging Eqs. (3.31) and (3.32) results in

$$\{\dot{\alpha}_n^m\} + \boldsymbol{V}[D][M]^{-1}\{\alpha_n^m\} = [M]^{-1}[D]\{\tau_n^m\} \tag{3.33}$$

$$-\{\dot{\delta}_n^m\} + \boldsymbol{V}[D][M]^{-1}\{\delta_n^m\} = [M]^{-1}[D]\begin{bmatrix} \ddots & & \\ & (-1)^{n+1} & \\ & & \ddots \end{bmatrix}\{\tau_n^m\} \tag{3.34}$$

The velocity above and on the rotor disc $\vec{v}_A$ is

$$\vec{v}_A(x, y, z, \bar{t}) = \alpha_n^0(\bar{t})\Phi_n^0(x, y, z) \tag{3.35}$$

where Φ_n^0, denoted as the shape function, is the product of the Legendre functions of the 1st and 2nd kind for the case of net thrust (m = 0):

$$\Phi_n^0(x, y, z) = \bar{P}_n^0(\nu)\, \bar{Q}_n^0(i\eta) \tag{3.36}$$

Both $\bar{P}_n^0$ and $\bar{Q}_n^0$ are dependent on the position perpendicular to the rotor, *z*, given the relationship between *x*, *y*, *z*, and *v*, η seen in Eq. 2.13:

$$\begin{aligned} x &= -\sqrt{1-\nu^2}\sqrt{1+\eta^2}\cos\Psi \\ y &= \sqrt{1-\nu^2}\sqrt{1+\eta^2}\sin\Psi \\ z &= -\nu\eta \end{aligned} \tag{2.13}$$

The velocity below the rotor disc $\vec{v}_B$ along the centerline is

$$\vec{v}_B(z,\bar{t}) = \vec{v}_A(0,\bar{t}-z) + \vec{v}^*(0,\bar{t}-z) - \vec{v}^*(-z,\bar{t}) \tag{3.37}$$

and the corresponding adjoint velocity $\vec{v}^*$ is

$$\vec{v}^*(z,\bar{t}) = \delta_n^0(\bar{t})\Phi_n^0(z) \tag{3.38}$$

Consequently, a multi-state system, the velocity above and on the rotor disc $\vec{v}_A$ along the centerline would then be

$$\vec{v}_A(z,\bar{t}) = \sum_{\boldsymbol{n=0}}^{\boldsymbol{N}} \alpha_n^0(\bar{t})\,\Phi_n^0(z) = \sum_{\boldsymbol{n=0}}^{\boldsymbol{N}} \alpha_n^0(\bar{t})\,\bar{P}_n^0(\nu)\,\bar{Q}_n^0(i\eta) \tag{3.39}$$

where *N* is the number of states within the system. Additionally, the velocity below the rotor disc $\vec{v}_B$ along the centerline, would be [2,8]

$$\vec{v}_B(z,\bar{t}) = \sum_{n=0}^{N} \alpha_n^0(\bar{t}-z)\,\Phi_n^0(0) + \sum_{n=0}^{N} \delta_n^0(\bar{t}-z)\,\Phi_n^0(0) - \sum_{n=0}^{N} \delta_n^0(\bar{t})\,\Phi_n^0(-z) \tag{3.40}$$

The combination of Eqs. (3.39) and (3.40) detail the inflow velocity everywhere in the flow field for an evolving wake, synonymous with Eq. (2.33) for the closed-form solutions.

To determine the inflow velocity for wake reversal, a modification is applied to Eqs. (3.39) and (3.40) similar to that applied to Eq. (2.33) to get the wake reversal velocity

distribution seen by Eq. (2.36). Specifically, the freestream velocity, instead of being a constant value of 1, now becomes a function of time $\bar{t}$ as shown in Eq. (2.34). The variable *z* is substituted for $z - s(\bar{t})$ in Eqs. (3.39) and (3.40), where $s(\bar{t})$ is defined by Eq. (2.35). Additionally, $\bar{t}$ is substituted by $\bar{t}_{stop}$ in the same fashion. These changes thus detail the inflow velocity everywhere in the flow field for a reversing wake:

$$\vec{v}_A(z,\bar{t}) = \vec{v}_A\big(z - s(\bar{t}), \bar{t}_{stop}\big) = \sum_{\boldsymbol{n=0}}^{\boldsymbol{N}} \alpha_n^0\big(\bar{t}_{stop}\big)\, \Phi_n^0\big(z - s(\bar{t})\big) \tag{3.41}$$

$$\begin{gathered}\vec{v}_B(z,\bar{t}) = \vec{v}_B\big(z - s(\bar{t}), \bar{t}_{stop}\big) = \\ \sum_{n=0}^{N} \alpha_n^0\big[\bar{t}_{stop} - \big(z - s(\bar{t})\big)\big]\, \Phi_n^0(0) + \sum_{n=0}^{N} \delta_n^0\big[\bar{t}_{stop} - \big(z - s(\bar{t})\big)\big]\, \Phi_n^0(0) \\ - \sum_{n=0}^{N} \delta_n^0\big(\bar{t}_{stop}\big)\, \Phi_n^0\big[-\big(z - s(\bar{t})\big)\big]\end{gathered} \tag{3.42}$$

Computationally, the state and co-state variables, α and δ respectively, must be saved at $\bar{t} = \bar{t}_{stop}$, as the wake generated prior to reversal is defined by the inflow coefficients at this given time.

3.7 Comparison of State-Space & Closed-Form Solutions

The following figures illustrate the velocity along the centerline of the rotor disc obtained using both the closed-form solution to the Potential Flow equations and the finite-state modeling. Specifically, the figures show the velocity at nondimensional time $\bar{t} = 10$, for multiple states of size *N*. Once again, for the states, α_n^m, and co-states, δ_n^m, *m* is set equal to 0 to correspond with the closed-form case in Chapter 2, where *m* = 0 and *n* = 1 for net thrust ($\tau_n^m = \tau_1^0 = \frac{2}{\sqrt{3}}$). However, *n* = *m*, *m+1*, *m+2*, … for the inclusion of more states for higher accuracy.

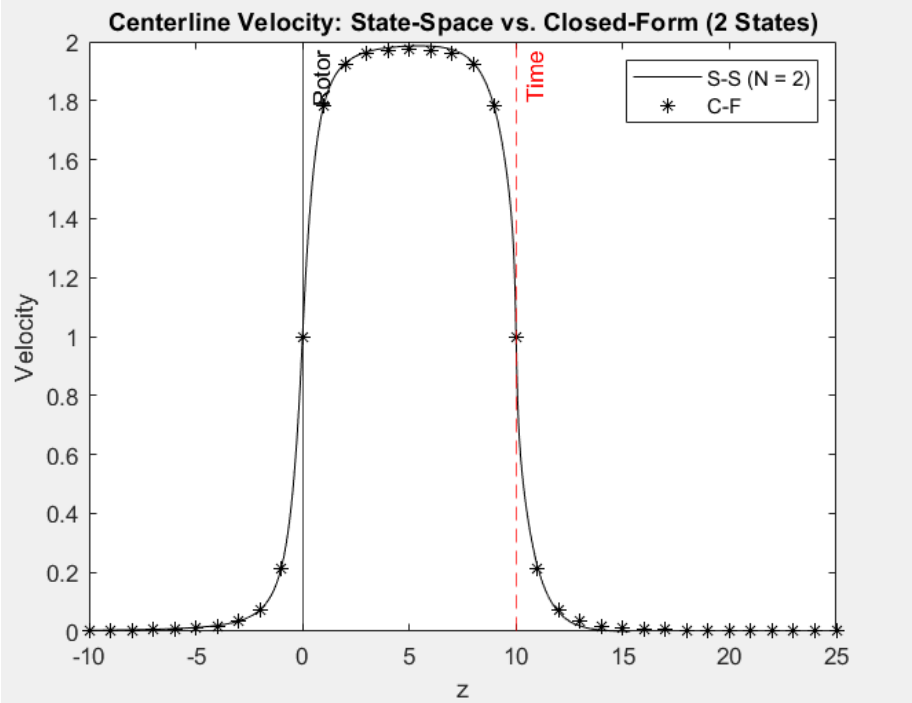
Centerline Velocity: State-Space vs. Closed-Form (2 States)
Velocity
z
Rotor
Time
S-S (N = 2)
C-F
2
1.8
1.6
1.4
1.2
1
0.8
0.6
0.4
0.2
0
-10
-5
0
5
10
15
20
25

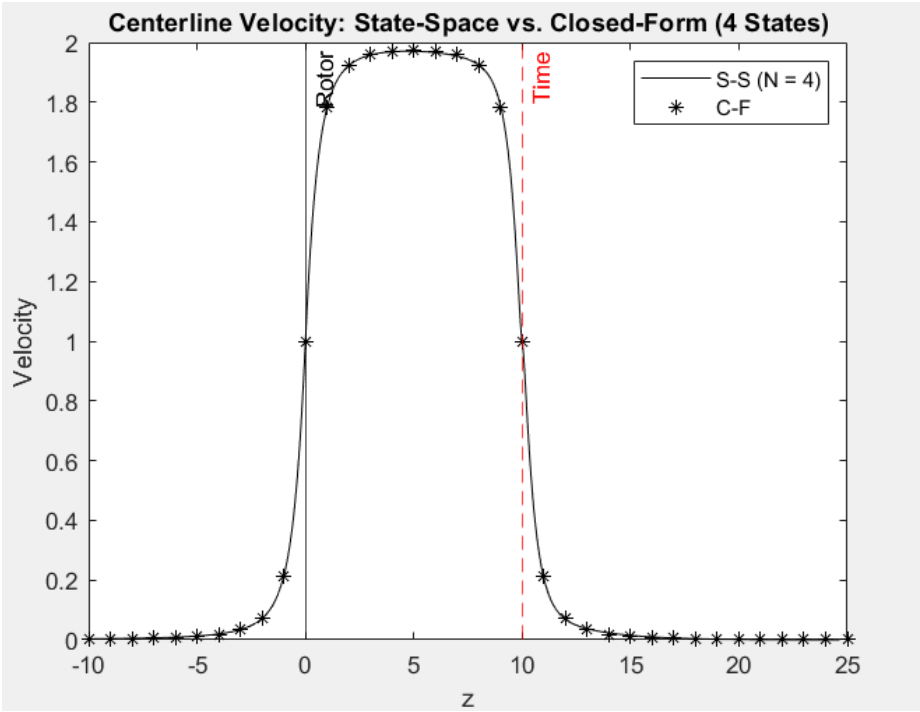
Centerline Velocity: State-Space vs. Closed-Form (4 States)
Velocity
z
Rotor
Time
S-S (N = 4)
C-F
2
1.8
1.6
1.4
1.2
1
0.8
0.6
0.4
0.2
0
-10
-5
0
5
10
15
20
25

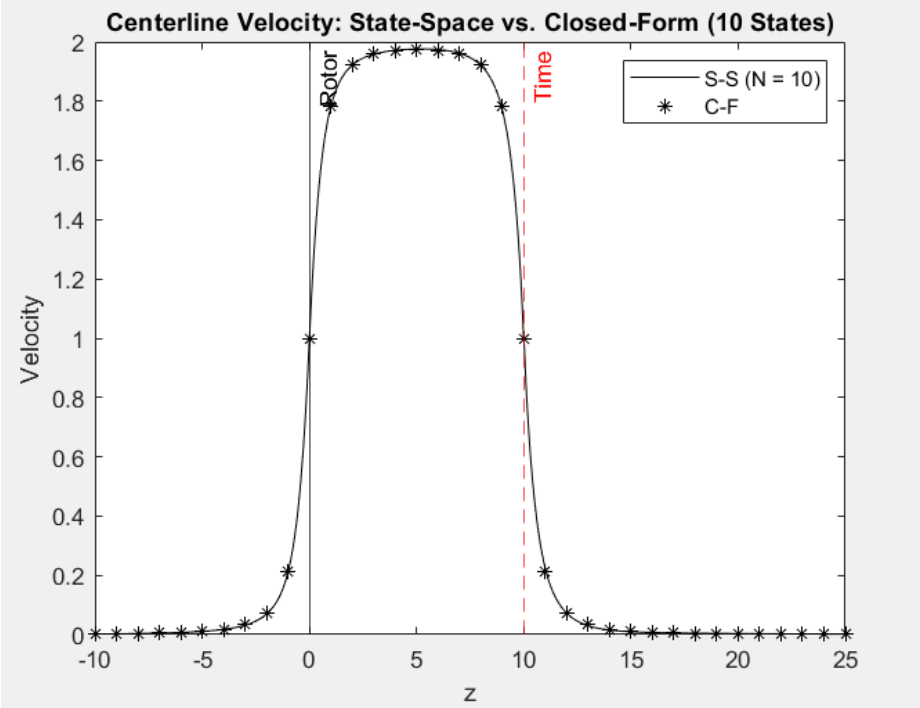

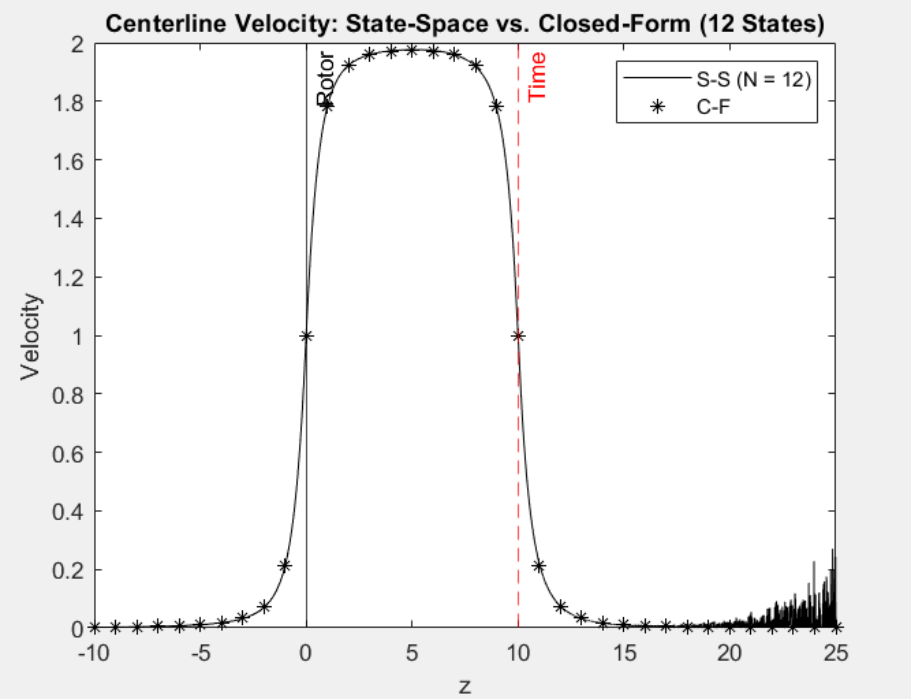

Figure 3.2 a-d. State-Space & Closed-Form Velocity Solutions for Helicopter In Climb

The resulting velocities determined by the closed-form and state-space methods agree quite well with each other, with any discrepancies between the two continuously diminishing with an increasing number of states. However, far downstream (as well as upstream) of the rotor,

numerical divergence occurs. This can be seen in Figure 3.2d where the state-space velocity begins to increasingly grow unstable for N = 12, beginning roughly at z = 20.

To determine the source of divergence for the finite-state solution, a detailed look at the numerical behavior of states and co-states was conducted. Additionally, the condition number, κ, was determined for matrices [M] and [D] to measure the ill-conditioned nature of the matrices as the number of states increases. The following figures highlight the states, α_n^0, to solve for the velocity above and on the disc, and the co-states, δ_n^0, to solve for the velocity below the disc for Figures 3.3 a-d:

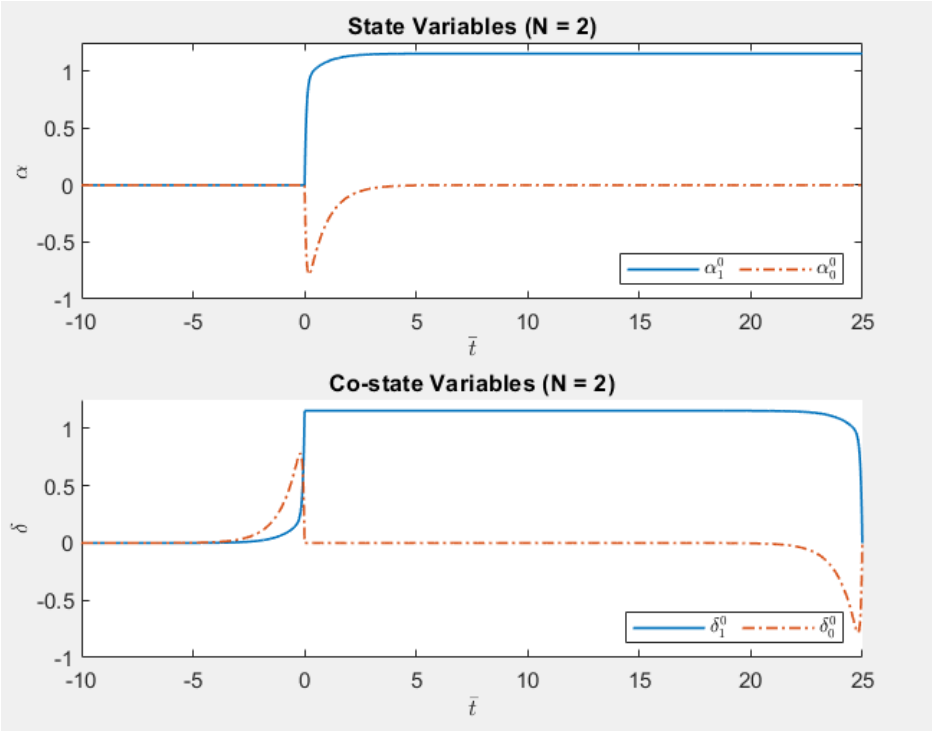

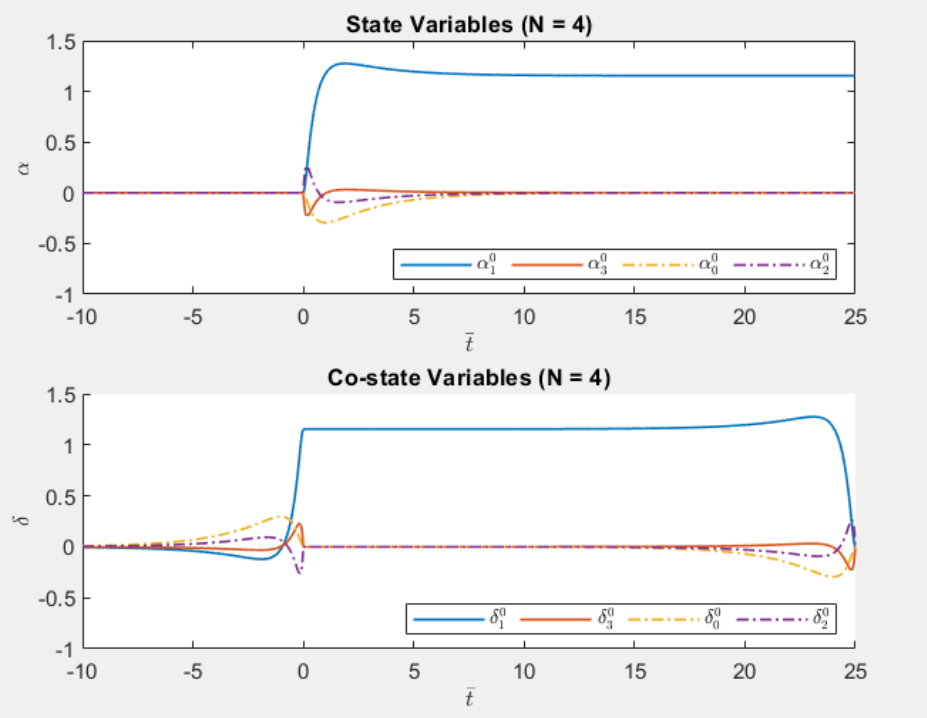
State Variables (N = 4)
α
$\bar{t}$
α_1^0 α_3^0 α_0^0 α_2^0
Co-state Variables (N = 4)
δ
$\bar{t}$
δ_1^0 δ_3^0 δ_0^0 δ_2^0

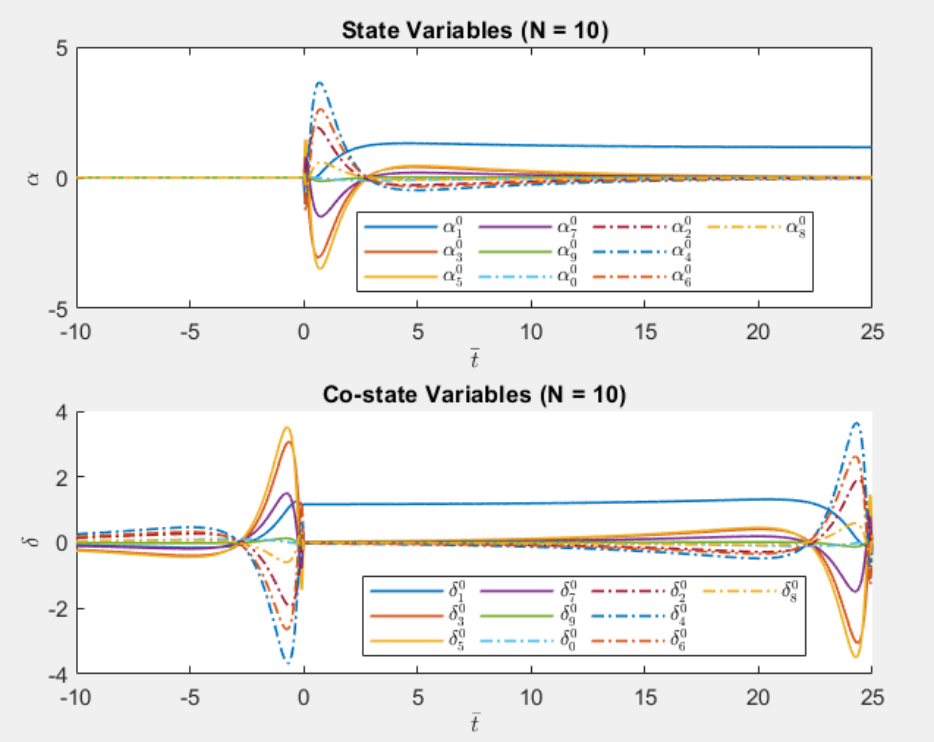
State Variables (N = 10)
α
$\bar{t}$
α_1^0 α_7^0 α_2^0 α_8^0
α_3^0 α_9^0 α_4^0
α_5^0 α_0^0 α_6^0
Co-state Variables (N = 10)
δ
$\bar{t}$
δ_1^0 δ_7^0 δ_2^0 δ_8^0
δ_3^0 δ_9^0 δ_4^0
δ_5^0 δ_0^0 δ_6^0

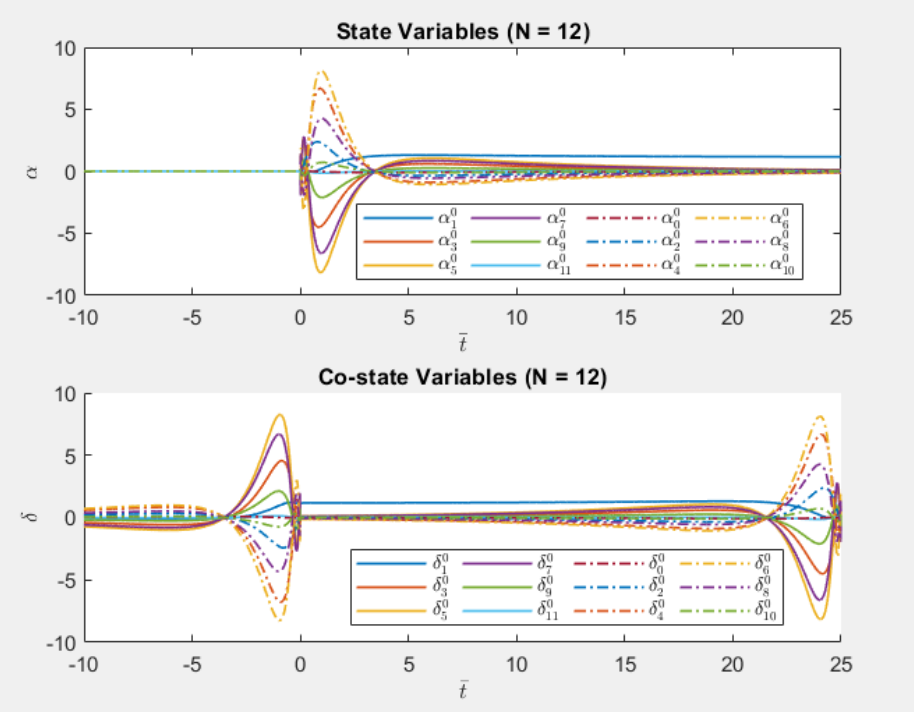

Figure 3.3 a-d. State and Co-State Variables for State-Space Velocities

The majority of the state variables have a stark increase at the initial time $\bar{t} = 0$ (they are all zero prior to $\bar{t} = 0$), followed by a progressive decrease to a steady-state solution to zero. The even-numbered states have a positive response shortly after $\bar{t} = 0$ before falling below zero and later approaching zero over time. Meanwhile the odd-numbered states have an opposite response to that of their even-numbered counterparts; they have a negative response shortly after $\bar{t} = 0$ before rising above zero and later approaching zero over time. The exception to this pattern is α_1^0, which only rises to a nonzero steady-state solution over time.

The co-state variables also follow a similar structure over time as the state variables when looking backwards in time starting at the final time ($\bar{t} = 25$), which is a result of the co-states being solved using backwards time-marching. However, yet another similar increase in the co-state response occurs again at $\bar{t} = 0$, with the sign of the co-states becoming flipped with respect

to time $\bar{t} = 25$. Once again, the exception to this pattern is δ_1^0, which rises to a nonzero steady-state solution over backwards time before rapidly approaching zero for $\bar{t} < 0$.

Looking at the state variables, α_n^0, as the number of states *N* increases, the magnitude of α_n^0 increases as well. This phenomenon also occurs for the co-state variables, δ_n^0. The increase in magnitude for the states and co-states with larger *N* suggest an ill-conditioned form of the state-space matrices. More direct evidence of [*M*] and [*D*] having an ill-conditioned nature is shown by viewing the condition number κ versus an increasing number of states. This can be seen in Figure 3.4 below:

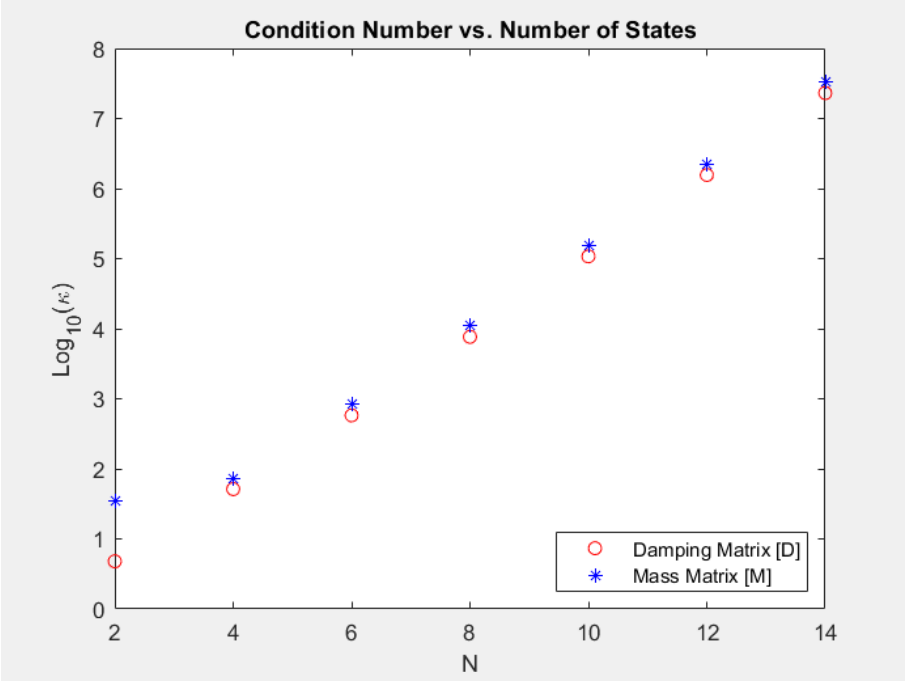

Figure 3.4. Condition Number vs. Number of States

The above plot shows condition number on a logarithmic (base 10) scale for matrices [*M*] and [*D*] as *N* increases by 2 (addition of both one even and one odd state) from 2 to 14. It can be seen that κ follows a very linear pattern with increasing *N*. As such, a linear fit for the condition numbers for both matrices was determined; these fits resulted in a slope of approximately 0.52

for the mass matrix and 0.5586 for the damping matrix (see Appendix B). Thus, the slopes imply that as the number of states increases by only 2, then the condition number increases by roughly 11 times for matrix [M] and 13 times for matrix [D], demonstrating that as the number of states increases, the corresponding chance of numerical divergence increases sharply. This divergence thereby occurs far from the rotor disc as round-off errors are most prevalent in this area [6]. However, the smaller round-off errors closer to the disc become noticeable as the states N increase due to the increasingly ill-conditioned matrix behavior.

3.8 Off-Axis Velocity Solutions

The resultant velocity solutions for a helicopter in climb in the previous section only details distributions along the centerline of the rotor disc. However, these distributions can be expanded off-axis to provide similar solutions over the entire disc. Additionally, considering the case of axial flow, the velocity at a given dimensionless radius, r, from the centerline is the same regardless of the azimuth angle, $\bar{\psi}$. The following figures show results of the off-axis velocities for both the closed-form and steady-state methods for r = 0.2, 0.5, and 0.8:

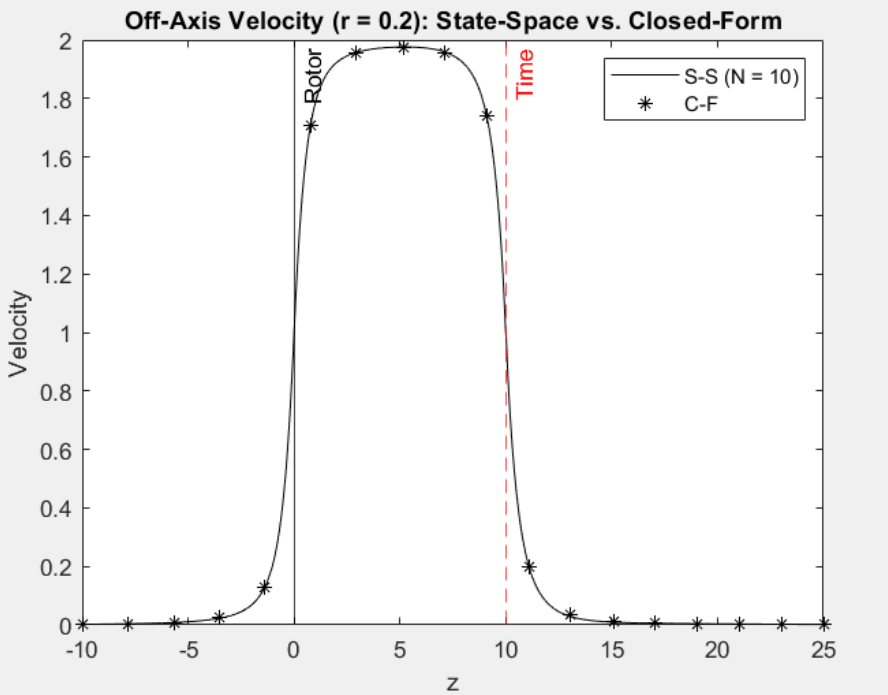
Off-Axis Velocity (r = 0.2): State-Space vs. Closed-Form
Rotor
Time
S-S (N = 10)
C-F
Velocity
z
2
1.8
1.6
1.4
1.2
1
0.8
0.6
0.4
0.2
0
-10
-5
0
5
10
15
20
25

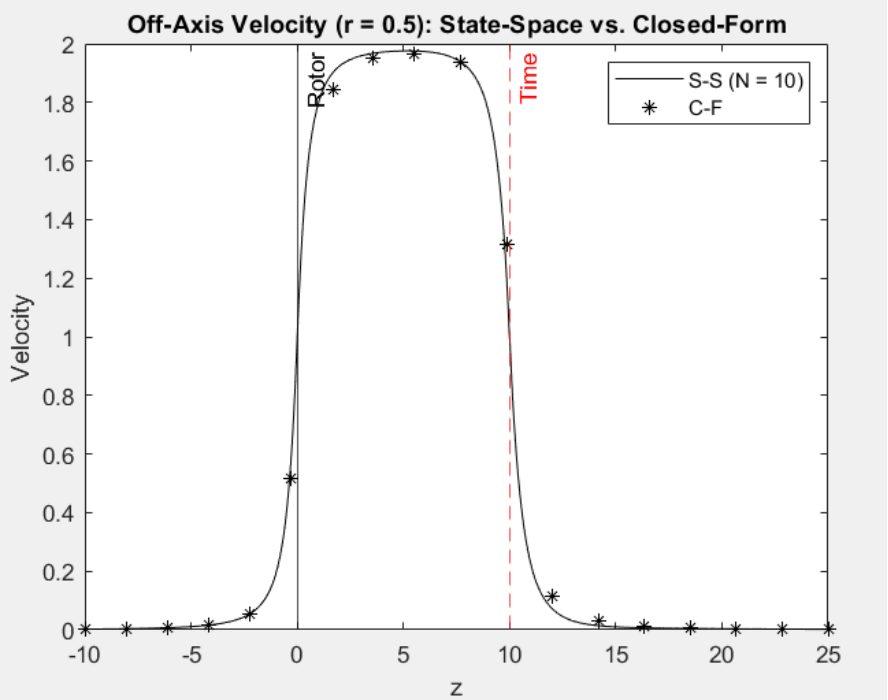
Off-Axis Velocity (r = 0.5): State-Space vs. Closed-Form
Rotor
Time
S-S (N = 10)
C-F
Velocity
z
2
1.8
1.6
1.4
1.2
1
0.8
0.6
0.4
0.2
0
-10
-5
0
5
10
15
20
25

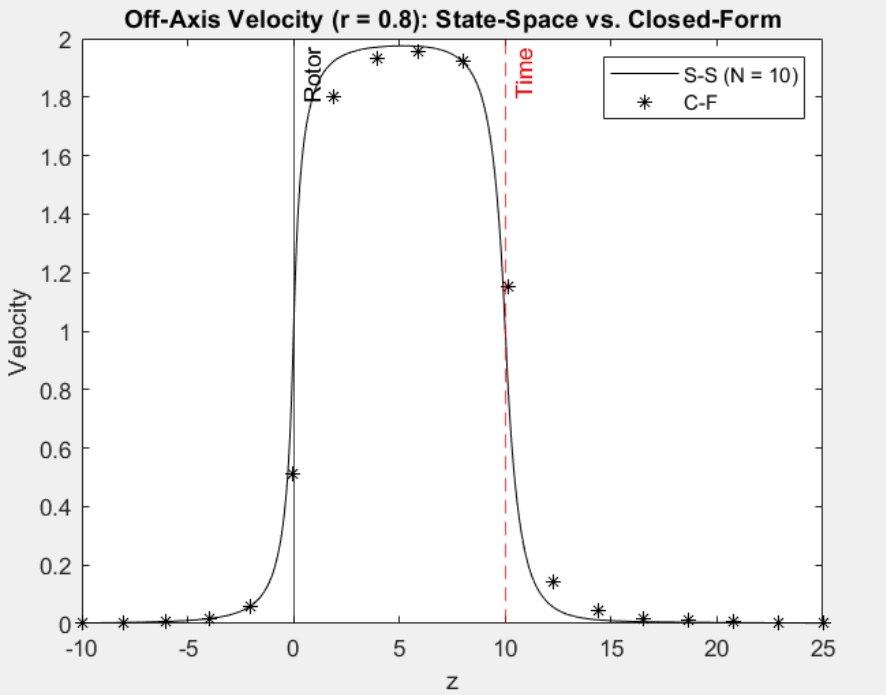

Figure 3.5 a-c. Off-Axis Velocity Response at Different Radii

From Figure 3.5, it can be seen that the velocity response for the state-space method and the closed-form method agree well with each other, similar to the results found along the centerline of the rotor disc. However, the degree to which the velocities of the two methods agree weakens when moving farther from the centerline. For r = 0.2, the state-space results match very closely with the closed-form results. However, slight deviation occurs at r = 0.5, and even more so at r = 0.8. The deviation between the two methods also occurs on and downstream of the rotor, with upstream results matching rather well regardless of the value of r.

3.9 Finite-State Velocity Solutions for Rotor Re-entry into Wake

Figure 3.6 below compares the finite-state and closed-form solutions for 10 states (N = 10) as the previously formed wake begins to translate downstream, then reverse direction and move back into the rotor disc (similar to the process shown in Figure 2.4). As the velocity of the wake only translates position with time, with no applied pressure to drive any additional velocity changes, the two solutions maintain the same convergence as demonstrated in Figure 3.2.

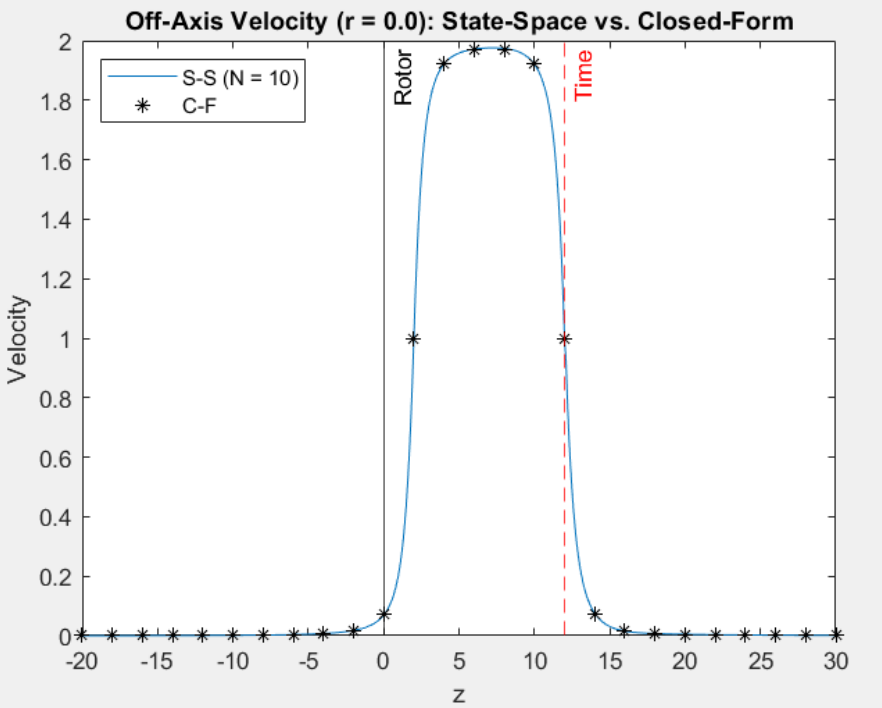
Off-Axis Velocity (r = 0.0): State-Space vs. Closed-Form
S-S (N = 10)
C-F
Rotor
Time
Velocity
z
2
1.8
1.6
1.4
1.2
1
0.8
0.6
0.4
0.2
0
-20
-15
-10
-5
0
5
10
15
20
25
30

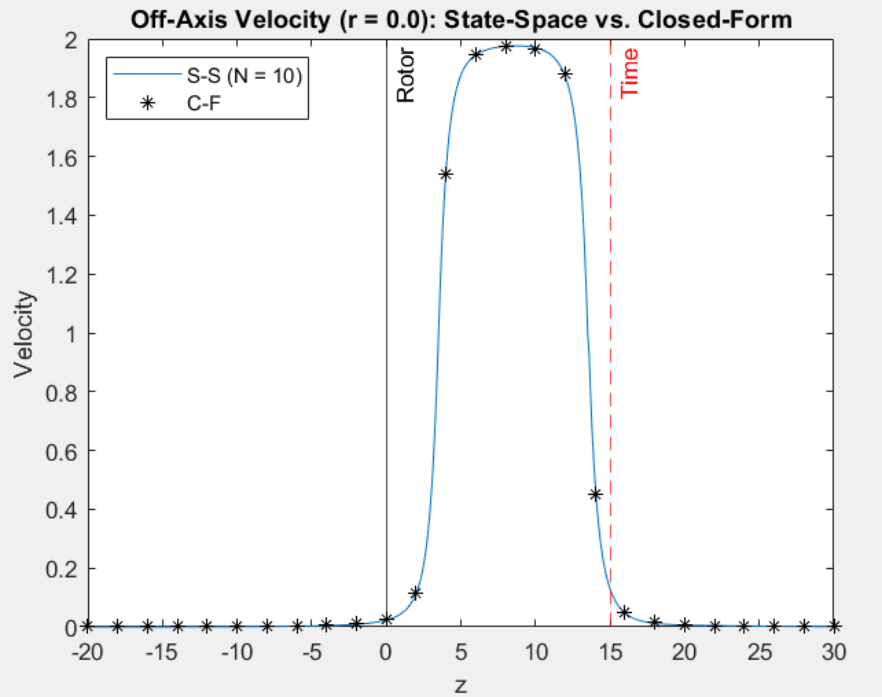
Off-Axis Velocity (r = 0.0): State-Space vs. Closed-Form
S-S (N = 10)
C-F
Rotor
Time
Velocity
z
2
1.8
1.6
1.4
1.2
1
0.8
0.6
0.4
0.2
0
-20
-15
-10
-5
0
5
10
15
20
25
30

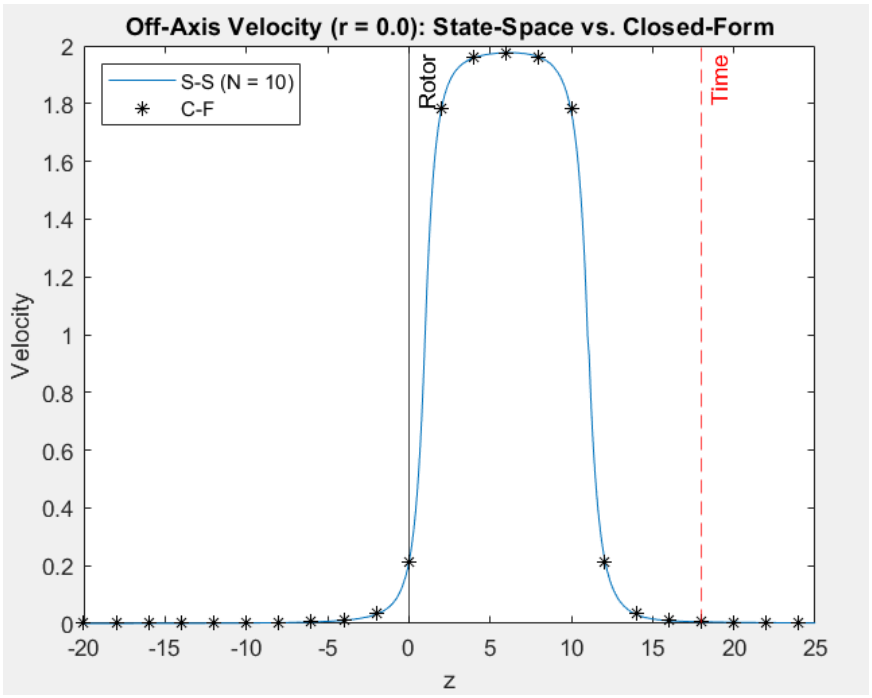
Off-Axis Velocity (r = 0.0): State-Space vs. Closed-Form
S-S (N = 10)
C-F
Rotor
Time
Velocity
z
2
1.8
1.6
1.4
1.2
1
0.8
0.6
0.4
0.2
0
-20
-15
-10
-5
0
5
10
15
20
25

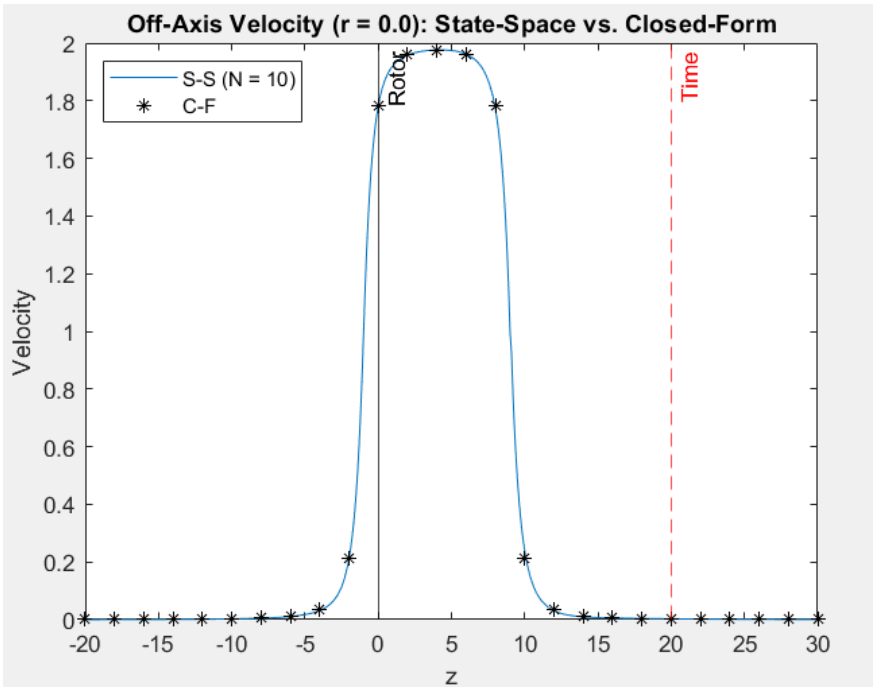
Off-Axis Velocity (r = 0.0): State-Space vs. Closed-Form
S-S (N = 10)
C-F
Rotor
Time
Velocity
z
2
1.8
1.6
1.4
1.2
1
0.8
0.6
0.4
0.2
0
-20
-15
-10
-5
0
5
10
15
20
25
30

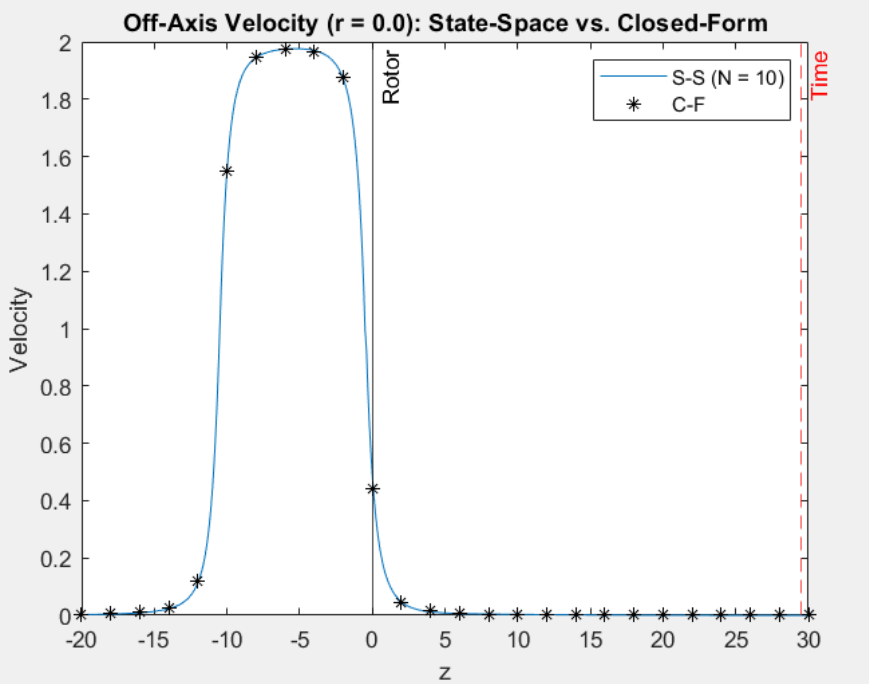

Figure 3.6 a-e. Finite-State Velocity Distribution: Growth, Translation, and Reversal

Chapter 4: Conclusions

4.1 Conclusions

Within this paper, a finite-state model simulating a single-rotor helicopter (assumed to be a rotor disc) reentering its own wake for the axial flow case was developed. The resultant velocity response of this model matches well with the closed-form velocity response for the same case. The finite-state model further agrees with the closed-form model as the number of states, N, increases. However, after $N = 10$, a numerical divergence occurs in the state-space velocity response resulting from round-off errors from the Legendre functions at large η, as well as the ill-conditioned nature of the matrices used to determine the states, α_n^0, and the co-states, δ_n^0. This numerical divergence initially begins far from the rotor disc (both upstream and downstream), but quickly approaches the disc with increasing N. Additionally, the finite-state model can be extended away from the centerline (axis) of the rotor disc, allowing for a determination of the velocity throughout the disc. These responses agree best at the rotor centerline ($r = 0$) and progressively agree less when approaching the edge of the rotor disc ($r = 1$).

References

[1] Peters, David A., "Hingeless Rotor Frequency Response with Unsteady Inflow," Proceedings of the American Helicopter Society Dynamics Specialists' Meeting, NASA Ames Research Center, NASA SP-352, February 1974, pp. 1-12.

[2] Seidel Cory, "Coupled Inflow and Structural Dynamics of Rotors with Time Delays and Adjoint Variables," PhD thesis, Washington University in St. Louis, 2020.

[3] Pitt, Dale M. and Peters, D. A., "Theoretical Prediction of Dynamic-Inflow Derivatives," *Vertica,* Vol. 5, No. 1, March 1981, pp. 21-34.

[4] Peters, David A., Boyd, David Doug, and He, Cheng Jian, "A Finite-State Induced-Flow Model for Rotors in Hover and Forward Flight," *Journal of the American Helicopter. Soc.*, Vol. 34, No. 4, Oct. 1989, pp. 5-17.

[5] Peters, David A. and Cao, Wen-Ming, "Off-Rotor Induced Flow by a Finite-State Wake Model," 37th AIAA SDM Conference, Salt Lake City, April 15-17, 1996, Paper No. 96-1550.

[6] Morillo, Jorge A. and Peters, David A., "Convergence of a Complete Finite-State Inflow Model of a Rotor Flow Field," 28th European Rotorcraft Forum, Bristol, England, September 17-20, 2002.

[7] Hsieh, Mong-che Antonio and Peters, David A., "Convergence and Conditioning of Dynamic Wake Models for Flight Dynamics," 31st European Rotorcraft Forum Proceedings, Florence, Italy, September 13-15, 2005.

[8] Fei, Zhongyang and Peters, David A. "A Rigorous Solution for Finite-State Inflow throughout the Flowfield—Including within the Wake," Proceedings of the AIAA 30th Applied Aerodynamics Conference, New Orleans, LA, June 25-28, 2012.

[9] Welsh, Jake and Peters, David A. "Foundations for Finite-State Modelling of a Two-Dimensional Airfoil that Reverses Direction," Masters thesis, Washington University in St. Louis, August 2022.

Appendix A: Galerkin Method

The Galerkin method is used to convert the momentum equation into a set of differential equations; the velocity potentials are expanded in terms of prime potentials, Ψ_n^m for this conversion. The test functions, λ_j^r, for the Galerkin are chosen to be the same Laplace solutions that are used as expansions for the pressure potentials:

$$\lambda_j^r = \phi_j^r = \bar{P}_j^r(v)\,\bar{Q}_j^r(i\eta) \qquad r = 0, 1, 2, \ldots, \infty \tag{A1.1}$$

$$\lambda_j^{rc} = \phi_j^{rc} = \phi_j^r \cos(r\bar{\Psi}) \tag{A1.2}$$

$$\lambda_j^{rs} = \phi_j^{rs} = \phi_j^r \sin(r\bar{\Psi}) \tag{A1.3}$$

Since the velocity potentials, Ψ, are only defined for the upper hemisphere (upstream from the rotor disc), integrations will only be done in the upper hemisphere, with all boundary conditions matched. Furthermore, the velocity solution is thus only valid above the disc.

After substitution of the expansions of pressure potentials, velocity potentials, and the expression of the velocity into the momentum equation, the gradient of the test functions are multiplied into the momentum equation, and a volume integration is performed over both sides. Use of the divergence theorem then allows the volume integrals to be expressed by surface integrals, and from the definition of the normal derivative of a function at a point on its length or surface, the surface integration in the plane of the rotor transforms to integration on the rotor disc, which has closed-form representations. This leads to a set of ordinary differential equations, with the cosine and sine functions being separated into two uncoupled sets. For the cosine parts, the Galerkin method gives:

$$\begin{bmatrix} [\tilde{L}^c]_{o,o} & [\tilde{L}^c]_{o,e} \\ [\tilde{L}^c]_{e,o} & [\tilde{L}^c]_{e,e} \end{bmatrix} \begin{Bmatrix} \{\dot{\hat{a}}_n^m\}_o \\ \{\dot{\hat{a}}_n^m\}_e \end{Bmatrix} + \begin{bmatrix} [D]^c_{o,o} & [D]^c_{o,e} \\ [D]^c_{e,o} & [D]^c_{e,e} \end{bmatrix} \begin{Bmatrix} \{\hat{a}_n^m\}_o \\ \{\hat{a}_n^m\}_e \end{Bmatrix} = \begin{bmatrix} [D]^c_{o,o} & [D]^c_{o,e} \\ [D]^c_{e,o} & [D]^c_{e,e} \end{bmatrix} \begin{Bmatrix} \{\tau_n^{mc}\}_o \\ \{\tau_n^{mc}\}_e \end{Bmatrix}$$

(A1.4)

where

$$[\tilde{L}^c] = \left[\iint_s \frac{\partial \Phi_j^{rc}}{\partial z}\left(\int_0^\infty \Phi_n^{mc}\, d\zeta\right) ds\right] = \left[\iint_s \Phi_j^{rc}\frac{\partial}{\partial z}\left(\int_0^\infty \Phi_n^{mc}\, d\zeta\right) ds\right] \tag{A1.5}$$

and

$$[D^c] = \left[\iint_s \frac{\partial \Phi_j^{rc}}{\partial z}\Phi_n^{mc}\, ds\right] = \left[\iint_s \Phi_j^{rc}\frac{\partial \Phi_n^{mc}}{\partial z} ds\right] \tag{A1.6}$$

for *m* = 0, 1, 2, … and *n* = *m+1*, *m+3*, *m+5*, … when *m+n* = *odd*, or *n* = *m*, *m+2*, *m+4*, … when *m+n* = *even*.). Note that the subscript "*o*" stands for the terms where *m+n* = *odd* and "*e*" stands for the terms where *m+n* = *even.* The sine components are similar to equation (A1.4).

The $[D]$ matrix for both the sine and cosine case is given by

$$D_{jn}^{rm} = \frac{1}{K_n^m}\delta_{jn}\delta_{rm} \qquad \begin{matrix} j+r = odd; & n+m = odd \\ j+r = even; & n+m = even \end{matrix} \tag{A1.7}$$

$$D_{jn}^{rm} = \frac{2\delta_{nm}}{\pi\sqrt{H_n^m H_j^m}}\frac{\sqrt{(2j+1)(2n+1)}}{(j+n+1)(j-n)}(-1)^{\frac{j+3n-1}{2}} \qquad \begin{matrix} j+r = odd; & n+m = even \\ j+r = even; & n+m = odd \end{matrix} \tag{A1.8}$$

The $[\tilde{L}]$ matrix is given by

$$\left[\tilde{L}_{jn}^{0m}\right]^c = X^m \Gamma_{jn}^{0m} \tag{A1.9}$$

$$\left[\tilde{L}_{jn}^{rm}\right]^{c} = \left[X^{|m-r|} + (-1)^{l} X^{|m-r|}\right] \Gamma_{jn}^{rm} \tag{A1.10}$$

$$\left[\tilde{L}_{jn}^{rm}\right]^{s} = \left[X^{|m-r|} - (-1)^{l} X^{|m-r|}\right] \Gamma_{jn}^{rm} \tag{A1.11}$$

$$X = \tan(\chi/2), \qquad l = \min(r, m) \tag{A1.12}$$

$$\Gamma_{jn}^{rm} = \frac{sign(r-m)}{\sqrt{K_n^m K_j^r}\sqrt{(2n+1)(2j+1)}} \delta_{j,n\pm1} \tag{A1.13}$$

r+m = odd; j+r = odd; n+m = odd
r+m = odd; j+r = odd; n+m = even

$$\Gamma_{jn}^{rm} = \frac{(-1)^{\frac{n+j-2r}{2}}(2)\sqrt{(2n+1)(2j+1)}}{\sqrt{H_n^m H_j^r}(n+j)(n+j+2)[(n-j)^2-1]} \tag{A1.14}$$

r+m = even; j+r = odd; n+m = odd

$$\Gamma_{jn}^{rm} = \frac{(-1)^{\frac{n+j-2r+2}{2}}(8)\sqrt{(2n+1)(2j+1)}}{\pi^2\sqrt{H_n^m H_j^r}(n+j)(n+j+2)[(n-j)^2-1]} \tag{A1.15}$$

r+m = even; j+r = even; n+m = even

$$\Gamma_{jn}^{rm} = \frac{(-1)^{\frac{3n+j-2m-2r}{2}}(4)sign(r-m)\sqrt{(2n+1)(2j+1)}}{\pi\sqrt{H_n^m H_j^r}(n+j)(n+j+2)[(n-j)^2-1]} \tag{A1.16}$$

r+m = odd; j+r = odd; n+m = even
r+m = odd; j+r = even; n+m = odd

$$\Gamma_{jn}^{rm} = \frac{1}{\sqrt{H_n^m H_j^r}\sqrt{(2n+1)(2j+1)}}\delta_{j,n\pm1} \qquad \text{(A1.17)}$$

r+m = even; j+r = odd; n+m = even
r+m = even; j+r = even; n+m = odd

Appendix B: Condition Number – Calculation and Linear Fit

The condition number (κ) of a matrix is defined as the ratio between the maximum and minimum eigenvalues (λ) of the matrix and is used as a measure the sensitivity that a function has to input errors. To determine κ for the [*M*] and [*D*] matrices, the "eig" MATLAB command was used to obtain the eigenvalues of the matrices at a specific number of states, then the ratio of the largest eigenvalue to the smallest eigenvalue was found. The table below details the aforementioned eigenvalues, in addition to the corresponding condition number.

Table B.1. Eigenvalues and Condition Numbers for Mass and Damping Matrices

		Number of States (*N*)						
		2	4	6	8	10	12	14
Mass Matrix [*M*]	λ_{max}	1.2157	1.8250	1.9756	2.0424	2.0898	2.1318	2.1707
	λ_{min}	0.0343	0.0250	0.0024	1.8677 E-04	1.3677 E-05	9.6422 E-07	6.6436 E-08
	κ	35.4718	72.9369	832.0081	1.0935 E04	1.5280 E05	2.2105 E06	3.2674 E07
Damping Matrix [*D*]	λ_{max}	1.8263	5.1567	8.8162	12.5964	16.4361	20.3107	24.2083
	λ_{min}	0.3811	0.1004	0.0152	0.0016	1.5264 E-04	1.2999 E-05	1.0491 E-06
	κ	4.7919	51.3757	579.3158	7.6470 E03	1.0768 E05	1.5625 E06	2.3075 E07

The resulting condition number for [*M*] and [*D*] at a given number of states can be seen in Figure 3.4. Linear fits to this data were applied in order to estimate the change in the condition number with increasing *N*. These fits can be seen in the following figure:

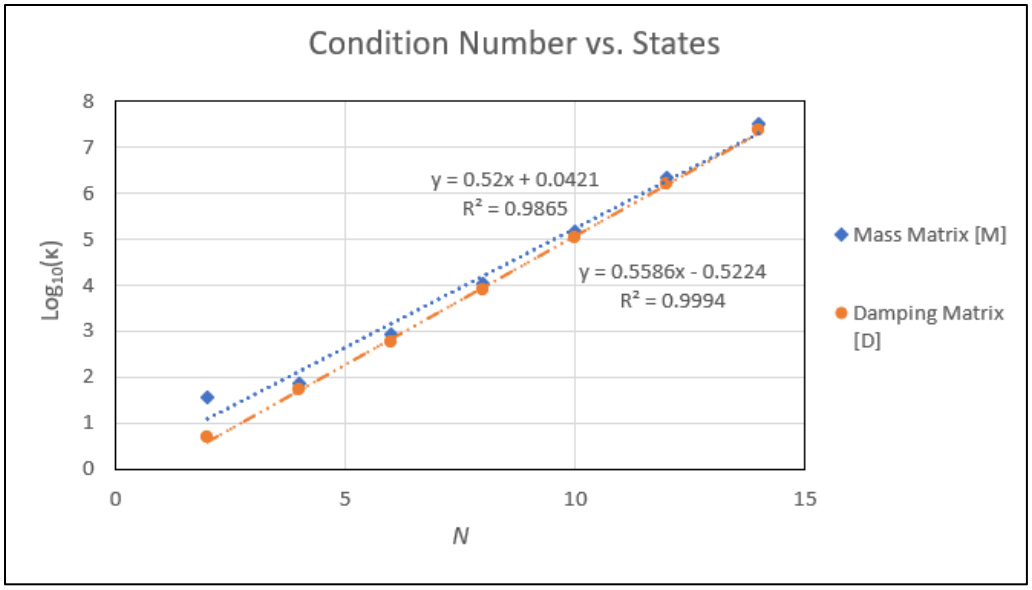

Figure B.1. Condition Number vs. N with Linear Fits (Excel)

Figure B.1 shows the linear fit with the corresponding condition number data for the mass and damping matrices on a log-base-10 scale. From these fits, it can be seen that the slopes of the $\log_{10}(\kappa)$ over N are 0.52 and 0.5586 for $[M]$ and $[D]$ respectively. Therefore, for every minimal increase in N, which would be an increase in 2 states to maintain matrix symmetry, then the increase in the condition number for $[M]$ and $[D]$ would be

$$Mass\ Matrix: \quad \log_{10}\left(\frac{\kappa_2}{\kappa_1}\right) = 0.52 * 2 \tag{B1.1}$$

$$Damping\ Matrix: \quad \log_{10}\left(\frac{\kappa_2}{\kappa_1}\right) = 0.5586 * 2 \tag{B1.2}$$

where κ_1 is the condition number at a given number of states N and κ_2 is the condition number at a given number of states $N+2$. From Eq. (B1.1) and (B1.2), the ratios between κ_1 and κ_2 are

$$Mass\ Matrix: \quad \frac{\kappa_2}{\kappa_1} = 10^{(0.52*2)} = 10.9648 \tag{B1.3}$$

$$Damping\ Matrix: \quad \frac{\kappa_2}{\kappa_1} = 10^{(0.5586*2)} = 13.0978 \tag{B1.4}$$

Thus, for every increase in the number of states from N to $N+2$, the condition number for the mass matrix increases by a magnitude of 10.9648, the condition number for the damping matrix increases by a magnitude of 13.0978. Therefore, the condition number for both matrices increase very quickly with an increase in the number of states, detailing the ill-conditioned nature of [M] and [D] for high values of N.